

AURORA AND AIRGLOW

Björn Gustavsson

March 1, 2023

Contents

| | |
|--|-----------|
| 1 Aurora and Airglow | 11 |
| 1.1 Introduction | 11 |
| 1.2 Emissions and Spectra | 12 |
| 1.2.1 Atomic Emissions, Transitions and Energy-levels | 13 |
| 1.2.2 Molecular Emissions, Energy-levels and Transitions | 14 |
| 2 Electron transport | 23 |
| 2.1 Electron impact Excitation | 23 |
| 2.2 Electron transport | 24 |
| 2.2.1 Electron Collisions | 25 |
| 2.3 Electron Transport Calculations | 30 |
| 2.3.1 Boltzmann Equation | 30 |
| 2.3.2 Transport equation | 31 |
| 2.3.3 Time-of-flight and steady-state | 31 |
| 2.3.4 Steady-state Electron Transport Calculations | 31 |
| 3 Aurora and Airglow - altitude and time-variations | 39 |
| 3.1 Auroral Emissions I | 39 |
| 3.2 Volume-Excitation-Rates | 39 |
| 3.3 Einstein coefficients and Lifetimes | 41 |
| 3.4 Forbidden Emissions | 42 |
| 3.5 Column-Emission-Rates | 46 |
| 3.6 Ionization-profiles | 47 |
| 3.6.1 Estimate of Primary Electron-spectra | 49 |
| 3.7 Monoenergetic spectra | 49 |
| 3.7.1 Typical electron-energy-spectra | 49 |
| 3.8 Ionization profiles for the “typical” spectra | 50 |
| 3.9 Auroral Red Line | 52 |
| 3.10 Production of $O(^1D)$ | 52 |
| 3.11 Production of $O(^1D)$ | 53 |
| 3.12 Altitude-profiles of 6300 Å volume-emission-rates | 54 |
| 3.13 Time-variation of $O(^1S)$ and the 5577 Å emission | 55 |
| 3.14 Molecular excitations | 58 |
| 3.15 Time-of-flight effects | 65 |

| | |
|--|-----------|
| 3.16 Effects on prompt emissions | 65 |
| 4 Precipitation-processes | 69 |
| 4.1 Diffuse Aurora | 69 |
| 4.1.1 Black Aurora | 71 |
| 4.2 Quasistatic Acceleration | 74 |
| 4.3 Alfvénic acceleration | 78 |
| 4.4 Other Auroras | 82 |

List of Figures

| | | |
|------|--|----|
| 1.1 | All-sky aurora | 12 |
| 1.2 | Conjugate Airglow-observations | 13 |
| 1.3 | Equatorial airglow | 13 |
| 1.4 | GLO VIS auroral spectra | 14 |
| 1.5 | Atomic Oxygen energy-levels | 15 |
| 1.6 | Molecular Nitrogen energy-levels | 16 |
| 1.7 | EUV-UV auroral spectra | 16 |
| 1.8 | Red-IR auroral spectra | 17 |
| 1.9 | Morse-potential | 20 |
| 1.10 | N ₂ triplet state vibrational energy level diagram | 21 |
| 1.11 | Temperature-variation of the N ₂ first positive 4-1 and 5-2 bands | 22 |
| 2.1 | Total cross-sections | 23 |
| 2.2 | Pitch-angle-resolved electron energy-flux | 24 |
| 2.3 | Electron collision cross-sections for O, N ₂ and O ₂ | 26 |
| 2.4 | Phase-functions | 27 |
| 2.5 | Cross-section measurement setup | 27 |
| 2.6 | electron-scattering geometry | 28 |
| 2.7 | electron-scattering geometry, part 2 | 29 |
| 2.8 | Secondary electron production-spectra | 29 |
| 2.9 | electron time-of-flight | 32 |
| 2.10 | Energy-level-diagram O and N ₂ | 34 |
| 2.11 | Photo-electron production | 34 |
| 2.12 | Two-stream electron-fluxes | 35 |
| 2.13 | Multi-stream electron-fluxes | 36 |
| 2.14 | Omnidirectional electron-fluxes | 37 |
| 3.1 | Altitude-profiles of volume emission-rates | 40 |
| 3.2 | O(¹ D) life-time profile | 43 |
| 3.3 | Steady-state-profiles of O ⁺ (2P) | 44 |
| 3.4 | Time-height-variation of O ⁺ (2P) | 45 |
| 3.5 | From volume to column emission | 47 |
| 3.6 | 6730 and 7774 Å column emission-rates | 48 |
| 3.7 | Ionization-profiles | 49 |
| 3.8 | Typical electron energy-spectra | 50 |

| | | |
|------|--|----|
| 3.9 | Ionization-profiles | 51 |
| 3.10 | Sources of O(1D) | 53 |
| 3.11 | Que-fig | 54 |
| 3.12 | Time-variation at 5577 Å | 56 |
| 3.13 | τ (O(1S)) | 58 |
| 3.14 | Ion recombination-times | 58 |
| 3.15 | 4 | 59 |
| 3.16 | N ₂ triplet state vibrational energy level diagram | 60 |
| 3.17 | 5 | 61 |
| 3.18 | Structure of the transition-matrix M | 62 |
| 3.19 | the inverse of the transition-matrix | 62 |
| 3.20 | Frank-Condon illustration | 63 |
| 3.21 | Frank-Condon N ₂ -triplets | 64 |
| 3.22 | 10 | 65 |
| 3.23 | Time-energy variation of electron fluxes | 66 |
| 3.24 | Altitude-time-variation of emission at 4278 Å | 66 |
| 3.25 | Elastic and inelastic cross-sections | 67 |
| 4.1 | Grouping of precipitation processes | 69 |
| 4.2 | Diffuse aurora, all-sky image | 70 |
| 4.3 | Small-scale diffuse aurora | 70 |
| 4.4 | FAST electron spectrogram | 71 |
| 4.5 | Diffuse auroral brightness and electron spectrograms | 72 |
| 4.6 | Black aurora | 72 |
| 4.7 | Pitch-angle-energy spectrogram of electrons above black aurora | 73 |
| 4.8 | Electron-spectra up and downward | 75 |
| 4.9 | Inverted-V precipitation | 76 |
| 4.10 | Horse-shoe distributed electrons | 77 |
| 4.11 | Cartoon | 77 |
| 4.12 | Alfven-wave velocity-profiles | 78 |
| 4.13 | Alfven-wave accelerated electron-spectra | 79 |
| 4.16 | Polar-cap arc | 81 |
| 4.17 | Cusp aurora, $B_z < 0$ | 82 |
| 4.18 | IMF control of cusp aurora | 83 |
| 4.19 | Cusp aurora, $B_z > 0$ | 84 |

List of Tables

| | | |
|-----|--|----|
| 1.1 | Atomic oxygen transitions | 15 |
| 1.2 | Molecular nitrogen data | 18 |
| 3.1 | Excited state and radiative life-time for a few prominent auroral emissions. | 41 |

Aurora and Airglow I
Emissions and Spectra Björn Gustavsson, Department of Physics, University of
Tromsø

Chapter 1

Aurora and Airglow

1.1 Introduction

In this chapter we will cover the physics of the optical emissions that are emitted from the upper atmosphere, that is the polar auroras and the airglow. The Aurora Borealis and Aurora Australis are the spectacular circumpolar light-phenomena that is caused by precipitation into the ionosphere-thermosphere from the magnetosphere that is the visible trace of the coupling between the solar-wind and magnetosphere to the upper atmosphere. The airglow is the optical emissions caused by other sources than particle precipitation - that is predominantly ion-chemistry. This chapter consists of four sections: Emission-spectra, electron-transport and excitation, altitude and time-variations, and particle acceleration and magnetosphere-ionosphere coupling. These sections are linked in the sense that they are processes of the aurora. However, they are also independent enough to be read in any order - provided the other aspects are temporarily taken as given: somehow by some mechanisms particles are made to precipitate from the magnetosphere into the thermosphere/ionosphere with high energies, somehow these particles move in the thermosphere where they ionize and excite atoms and molecules with some altitude and time-variation, then these excited atoms and molecules emit photons at some combinations of wavelengths.

Aurora and Airglow are optical emissions from excited atoms, molecules and ions in the upper atmosphere - typically from the mesopause-region and above. Aurora are emissions produced directly or indirectly by energetic particles (electrons and protons) precipitating from the magnetosphere down into the atmosphere, while airglow are produced directly (resonant scattering) or indirectly (excitation by photo-electrons, chemical reactions) by solar radiation. Light with wavelength as short as 900 Å all through to the far IR are produced - the EUV aurora are not visible from ground (due to atmospheric absorption) but is dominant as observed from space - also in some aspects better suitable for observations from space since the lower atmosphere and ground is dark in the far UV-part of the spectrum (also due to atmospheric absorption). This allows observations on the sunlit dayside.

1.2 Emissions and Spectra

- Aurora - particle impact production (e^- , H^+)
- Airglow - Solar radiation (by way of photo-electrons, chemistry...)

The night-sky is not black on planet Earth. At high latitudes precipitation of high-energy particles, mainly electrons but also protons, cause ionization and production of secondary electrons at energies from 0 to a couple of 100 electron-volts, these energetic electrons collide elastically and inelastically with the neutral atmosphere producing atoms and molecules in excited states, that then emit light which we see as aurora (see figure 1.1). At lower latitudes where there is no energetic particle precipitation there is airglow (see figures 1.2 and 1.3), that is emissions from atoms and molecules in the thermosphere–upper mesosphere, produced in exothermic chemical reactions. The energy leading to airglow originates from the extreme UV radiation from the sun, that is reservoired in the thermosphere–ionosphere. Ions, electrons and, for example, oxygen atoms have ionization and chemical bonding-energy that can be released in recombination and chemical reactions. Since the ionization energy of O_2^+ is just above 12 eV dissociative recombination of molecular oxygen ions have enough energy to leave the resulting atoms in excited states, other exothermic reactions can too.

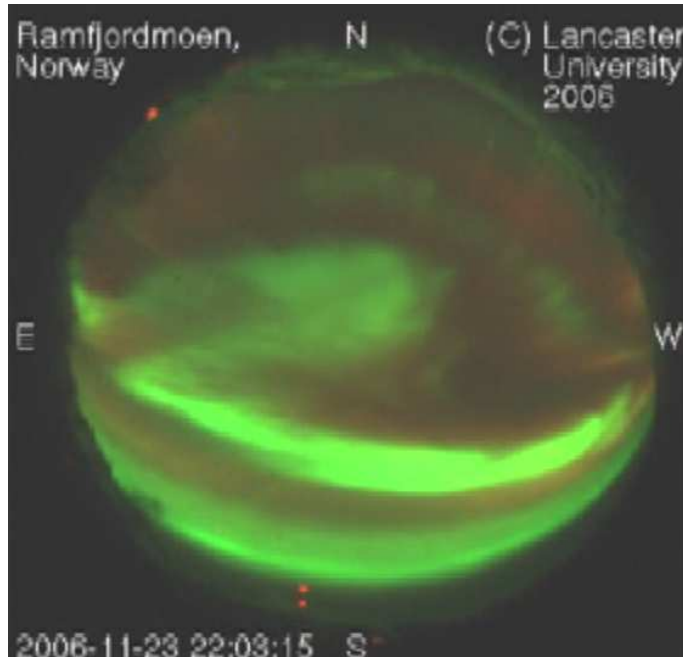


Figure 1.1: A typical all-sky auroral display observed with the DASI imager operated in Ramfjordmoen, Tromsø, Norway, by Lancaster University. Used by courtesy of *M Kosch*

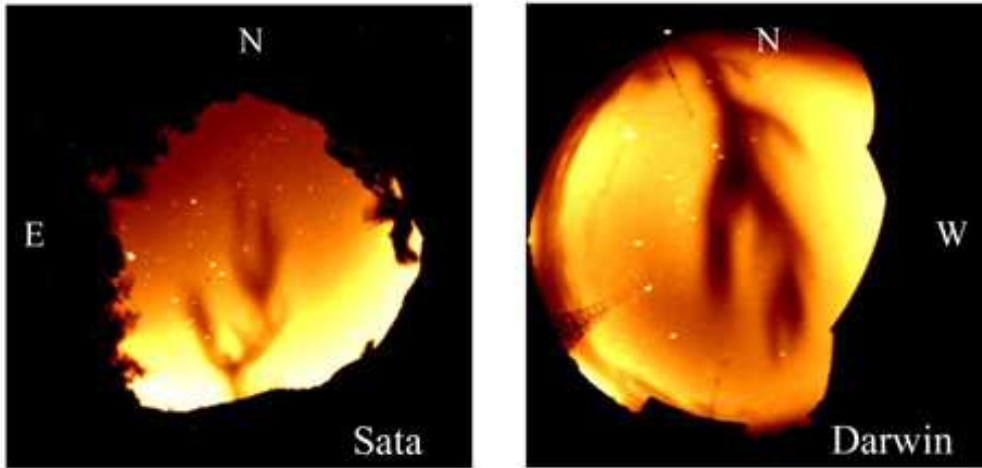


Figure 1.2: Airglow-observations in the $6300 \text{ \AA} O(^1D)$ emission from Sata in southern Japan, to the left, and Darwin in northern Australia, *Otsuka et al.* [from 2002], show structures from by equatorial bubbles caused by Rayleigh-Taylor instabilities in the bottom-side equatorial F-region.

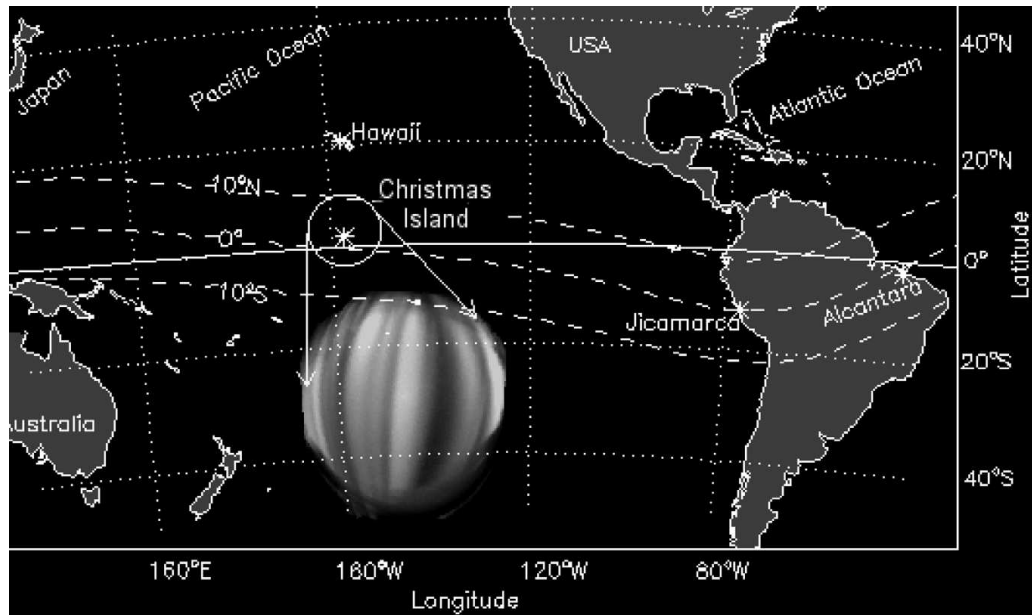


Figure 1.3: Airglow image from the Christmas Island showing the norht-south extent of equatorial plasma-bubbles.

1.2.1 Atomic Emissions, Transitions and Energy-levels

The photons emitted from excited atoms are/produced/occur at discrete wavelengths corresponding to the energy-elevel separation between the excited state

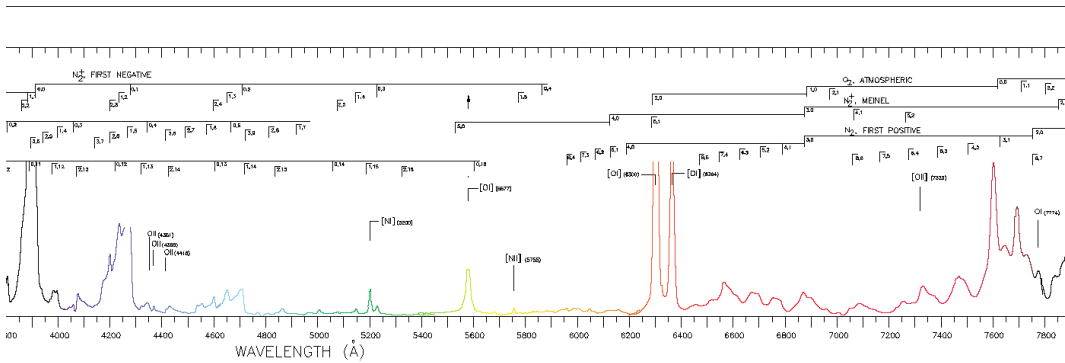


Figure 1.4: Zoom-in on the visible part of the GLO-spectra. The visible part of the auroal spectra is dominated by the atomic oxygen emission-lines at 5577 and 6300 Å and the molecular emission-bands from molecular nitrogen in red and molecular nitrogen ions in the blue-violet.

and the lower state, see for example the discrete emission-lines at 5577, 6300 and 6364 Å in figure 1.4. These three emission-lines originate from atomic oxygen in the $O(^1S)$ and $O(^1D)$ states, see figure 1.5. The width of the lines are caused by natural line-broadening by Doppler-widening due to thermal motion of the atoms and the natural line-width due to the life-time of the upper state and by the resolution of the spectrograph. What transitions are possible from an excited atom are determined by quantum mechanics. That photons are produced with spin 1 set the constraints on the possible spin-differences between the wavefunctions before and after the photon emission and symmetry of the quantum-mechanical transition operators (electrical dipole, magnetic dipole, electrical quadrupole etc.) gives us the selection-rules for transitions. For our purposes we can take the transition-probabilities, or Einstein coefficients, from laboratory experiments. In the upper atmosphere the collision-frequencies are low enough that transitions can occur between states that are electric-dipole-“forbidden”. Allowed transitions are electrical dipole transitions, typically with radiative life-times on the order of micro-seconds or shorter. Electric-dipole-forbidden transitions can still occur due to magnetic dipole or electrical quadrupole transitions. However, for these the Einstein coefficients are much smaller and the life-time becomes correspondingly longer. For the atomic oxygen emissions at 5577, 6300, 7774 and 8446 Å the the green and red lines are forbidden while the IR-emission are allowed, see table 1.2.

1.2.2 Molecular Emissions, Energy-levels and Transitions

Just as atoms molecules too have electronically excited states. In figure 1.6 selected energy-levels of molecular nitrogen and molecular nitrogen ions are displayed together with the prominent emissions between them.

However, when looking at the wave-lengths corresponding to the energy-separation between the electronically excited states of molecular nitrogen, molecular oxygen and

Table 1.1: Probabilities for atomic oxygen transitions between the 1S , 1D , 3P , levels, all data are taken from the review by *Itikawa and Ichimura* [1990].

| Transition | λ (Å) | A (s^{-1}) | τ (s) |
|-----------------|---------------|------------------------|--------------------|
| $^1S_0 - ^3P_2$ | 2958 | $2.732 \cdot 10^{-4}$ | |
| $^1S_0 - ^3P_1$ | 2972 | $7.601 \cdot 10^{-2}$ | |
| $^1S_0 - ^1D_2$ | 5577 | 1.215 | |
| 1S_0 | | 1.291 | 0.7744 |
| $^1D_2 - ^3P_2$ | 6300 | $5.626 \cdot 10^{-3}$ | |
| $^1D_2 - ^3P_1$ | 6364 | $1.818 \cdot 10^{-3}$ | |
| $^1D_2 - ^1P_0$ | 6492 | $8.922 \cdot 10^{-7}$ | |
| 1D_0 | | $7.445 \cdot 10^{-3}$ | 134 |
| $^3P_0 - ^3P_2$ | 440600 | $1.203 \cdot 10^{-10}$ | |
| $^3P_0 - ^3P_1$ | 1455000 | $1.725 \cdot 10^{-5}$ | |
| 3P_0 | | $1.725 \cdot 10^{-5}$ | $5.764 \cdot 10^4$ |
| $^3P_1 - ^3P_2$ | 631900 | $8.957 \cdot 10^{-5}$ | |
| 3P_1 | | $8.957 \cdot 10^{-5}$ | $1.116 \cdot 10^4$ |

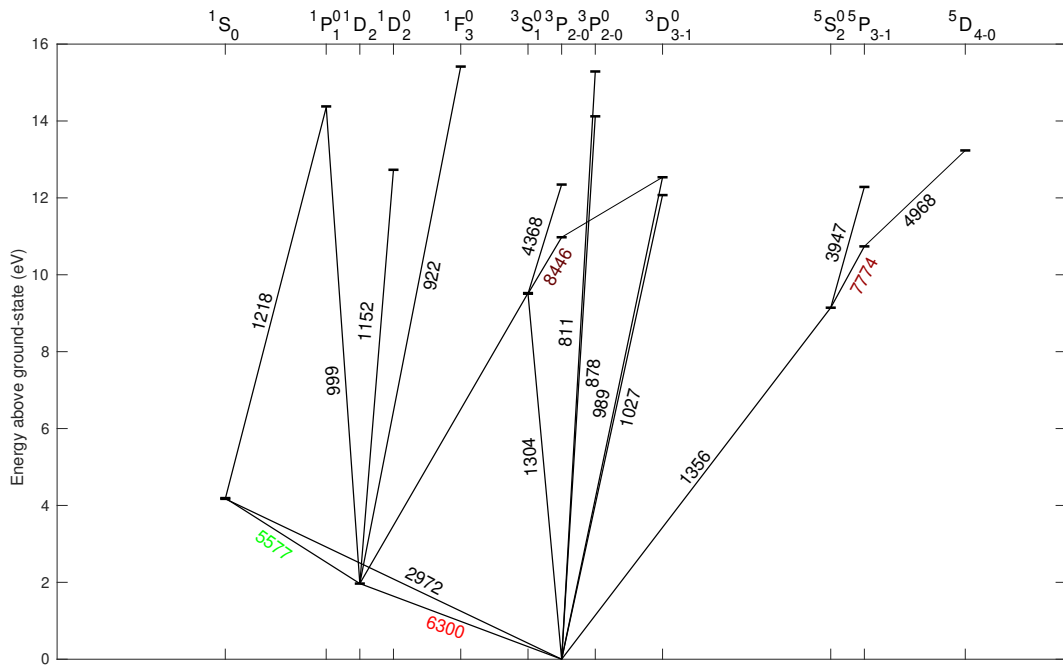


Figure 1.5: Partial energy-level diagram of atomic oxygen, adapted from *Rees* [1989].

their ions there are not similar discrete lines, see figures 1.7 and 1.8. This is because diatomic molecules have additional degrees of freedom, both vibrations and rotations, therefore the quantum-mechanics becomes more intricate and complicated (larger molecules are outside the scope of auroral physics).

Fortunately the electronic part of the Schrödinger-equation separates from the

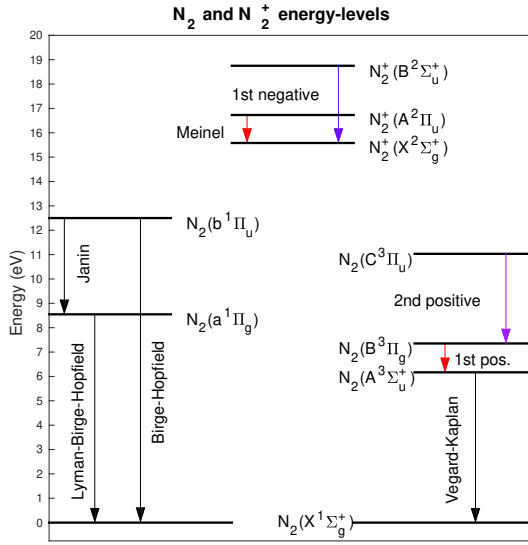


Figure 1.6: Partial energy-level diagram for the electronic states of molecular nitrogen.

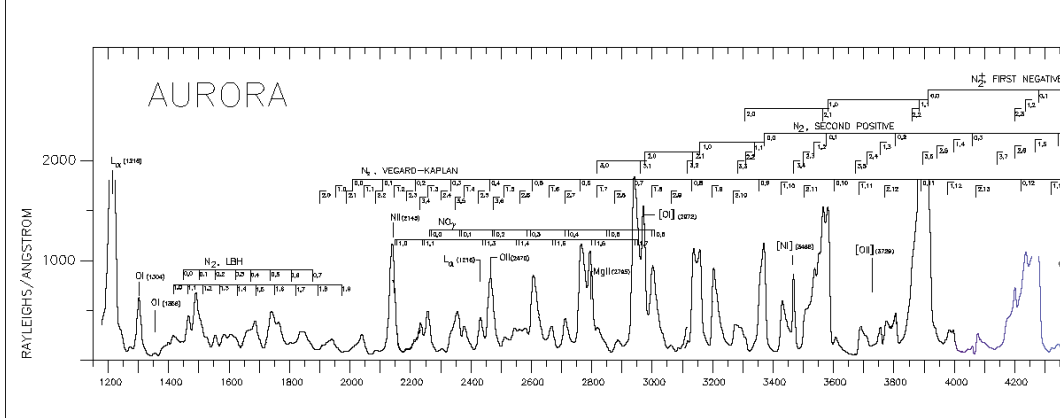


Figure 1.7: The extreme ultraviolet part of the spectra contains several strong atomic emission-lines, notably Lyman- α and β at 1026 and 1216 Å, as well as atomic-oxygen emissions, for example at 1304 Å. At slightly longer wavelengths the spectra is dominated by the N_2 Lyman-Birge-Hopfield, Vegard-Kaplan and Second Positive bands and the N_2^+ First Negative bands, as can be seen in the GLO spectra.

vibrational and rotational parts - that is the energy-levels of the electronic states are independent of the vibrational and rotational excitation. Further the vibrational potential depends on the electronic excitation but is independent of the rotational excitation. The energy of emitted photons will be the sum of the difference between the energy of the electronic vibrational and rotational states of the transition. Typically the energy-difference between excited electronic states are on the order of 1 eV, while the difference between vibrational states are on the order of 0.1 eV and the rotational states have a separation of 0.01 eV or smaller. Both the vibrational and

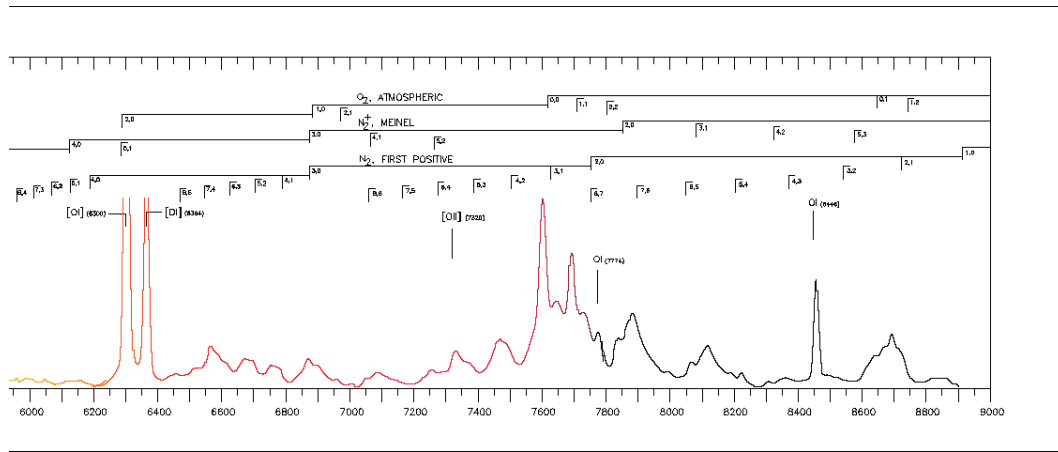


Figure 1.8: The red-IR part of the auroral spectra contains a couple of strong atomic oxygen emission-line at 6300, 6364, 7774 and 8446 Å, O⁺ at 7320-7330 Å and the N₂ Meinel and First Positive bands.

rotational motions are quantized. transition-rules still applies - since photons still escape with spin 1. With the possible change in vibrational and rotational level the total energy of emitted photons will be distributed in a sequence (vibrational step) of bands (rotational step).

The vibrational motion is similar to the ideal harmonic quantum-mechanical oscillator, where the force of the molecular bond depends on the deviation from the equilibrium separation distance between the atoms. The atoms will oscillate around the potential minima with an approximately harmonically. However, since the molecular bond has a finite energy, the dissociation energy, the potential of the vibrational motion has to approach that energy for large atomic separations (the energy needed to pull the atoms apart and break the molecular bond). A potential describing the energy of a two-atom-system vibrating should level off at the dissociation-energy – that is at large enough internuclear separation the molecular bond will be broken, the energy required to separate the atoms that far should correspond to the disocciation energy. The energy of the atoms should increase rapidly when the internuclear separation decreases – due to the increasing overlap between the electron-wave-functions and the repelling Coulomb-force between the atomic nuclei. An assymetric potential that models this reasonably well is the Morse-potential:

$$V(r) = D_e \left(1 - e^{-a(r-r_e)}\right)^2 \quad (1.1)$$

where D_e is the dissociation-energy, r_e is the equilibrium separation between the atoms, and a is a sharpness-parameter. the potential $V(r)$ increases exponentially when the separation, r becomes smaller than r_e , and when r increases $V(r)$ increases to D_e . There is a finite number of bound vibrational levels and their discrete energy-

Table 1.2: Data for molecular nitrogen, in the ground-state and the major electronically excited triplet-states, all data are taken from the review by *Itikawa et al.* [1986].

| Excited-state | r_e ^a (Å) | E_0 ^b (eV) | D_e ^c (eV) | $\Delta E_{vib}(0 - 1)$ ^d (eV) | a^e (/Å) |
|-----------------------|---------------------------|----------------------------|----------------------------|--|---------------|
| $N_2(C^3\Pi_u)$ | 1.149 | 11.032 | 1.111 | 0.2476 | 11.064 |
| $N_2(B'^3\Sigma_u^-)$ | 1.278 | 8.1647 | 5.170 | 0.1851 | 3.4066 |
| $N_2(W^3\Delta_u)$ | 1.28 | 7.3622 | 4.781 | 0.1833 | 3.5128 |
| $N_2(B^3\Pi_g)$ | 1.2126 | 7.3532 | 4.79 | 0.2114 | 4.06 |
| $N_2(A^3\Sigma_u^+)$ | 1.2866 | 6.1688 | 3.590 | 0.1777 | 3.9535 |
| $N_2(X^1\Sigma_g^+)$ | 1.0977 | 0 | 9.759 | 0.28887 | 3.857 |

^aInternuclear equilibrium distance.

^bEnergy of the lowest vibrational state relative to $N_2(X^1\Sigma_g^+, \nu = 0)$.

^cDissociation energy.

^dEnergy difference between the vibrational states with $\nu = 0$ and $\nu = 1$.

^eCalculated to fit Morse-potential energy-levels with $\Delta E_{vib}(0 - 1)$, the relative error of the vibrational energy-levels of the Morse-potential increases up to approximately 3 per cent at $\nu = 21$, for accurate work on N_2 spectra turn to *Gilmore et al.* [1992].

levels are:

$$E_n = h\nu_0(n + 1/2) - \frac{[h\nu_0(\nu + 1/2)]^2}{4D_e} \quad (1.2)$$

where $\nu_0 = \frac{a}{2\pi}\sqrt{2D_e/m}$. The spacing between the vibrationally excited states decrease with increasing vibrational level. The spacing between vibrational levels depends on how sharp the Morse-potential is and this varies for different electronically excited states. For molecular nitrogen the energy-difference between the vibrational states with $\nu = 0$ and $\nu = 1$ varies according to table 1.2

In reality the oscillations are little bit more complicated and for accurate modeling of the emission-spectra from molecules the Morse-long-range-potential is typically used, it includes additional free parameters that can be adjusted such that transitions between vibrational levels accurately reproduce observed spectra.

The rotational energies are reasonably well modeled with a rigid two-body rotating system where the rotational energy-levels can be modeled with

$$E_J = B_\nu J(J + 1) - D_\nu J^2(J + 1)^2 \quad (1.3)$$

where J is the rotational quantum-number and B_ν and D_ν are the rotational parameters, that depend weakly on the vibrational level ν .

For $N_2(X^1\Sigma_g^+)$ $\Delta E_\nu(0 - 1) \approx 0.29$ eV, and $\Delta E_J(0 - 1) \approx 0.001$ eV. Rotational states have small enough energy-separation to be excited by thermal motion of the molecules - recall that 0.1 eV corresponds to approximately 1000 K and with thermospheric temperatures of 700 K the 0.28 eV energy of the first vibrationally excited state of N_2 is at 4 thermal energies above the 0-th vibrational level. The rotational states with their 0.001 eV energy-separation, however, are thermally populated. For

transitions between two states the change of the rotational quantum-number is either -1, 0 or 1. These give rise to the P-branch ($\Delta J = -1$), the R-branch ($\Delta J = 1$) and the Q-branch ($\Delta J = 0$). The set of selection rules that governs the emission are somewhat convoluted. If both upper and lower electronic states involved in the transition have no electronic angular momentum component along the molecular axis (i.e. the electronic Σ -states), then $\Delta J = \pm 1$ (i.e. no Q-branch). For all other transitions $\Delta J = 0, \pm 1$. Further a transition cannot occur from $J = 0$ state to another $J = 0$ state. This means that no line appears at the band origin for the Q-branch. Selection rules arise from quantum-mechanics of the photon-emission and are a product of the transition-operator (electrical dipole, magnetic dipole, electrical quadrupole etc) and the wave function symmetries, which yields a non-zero value only under certain conditions.

In the visible part of the spectrum there are four electronic transitions from N_2 and N_2^+ that are particularly strong, the first and second positive bands from N_2 and the Meinel and first negative bands from N_2^+ . The first positive band is dominant in the red part and the first negative band dominates in the blue–near UV part of the spectrum.

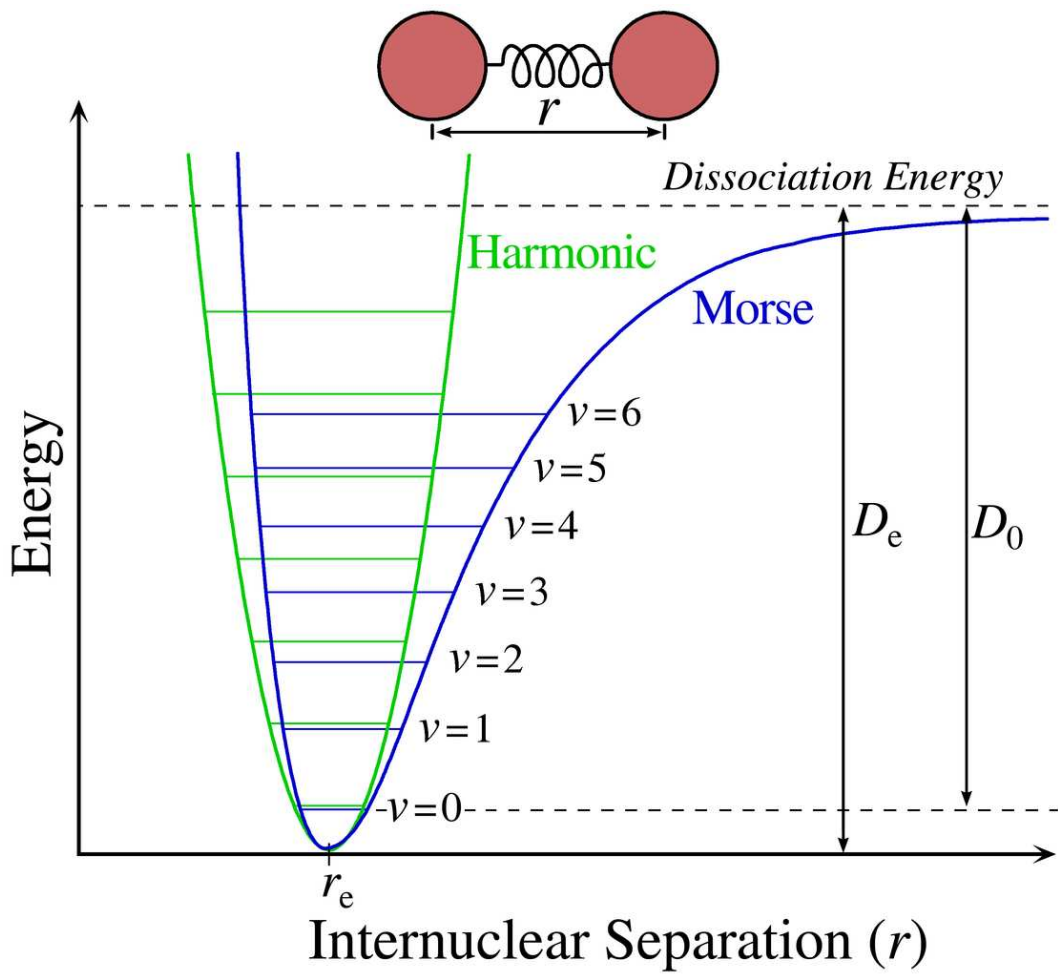


Figure 1.9: The Morse-potential is a reasonably accurate potential for vibrations in di-atomic molecules.

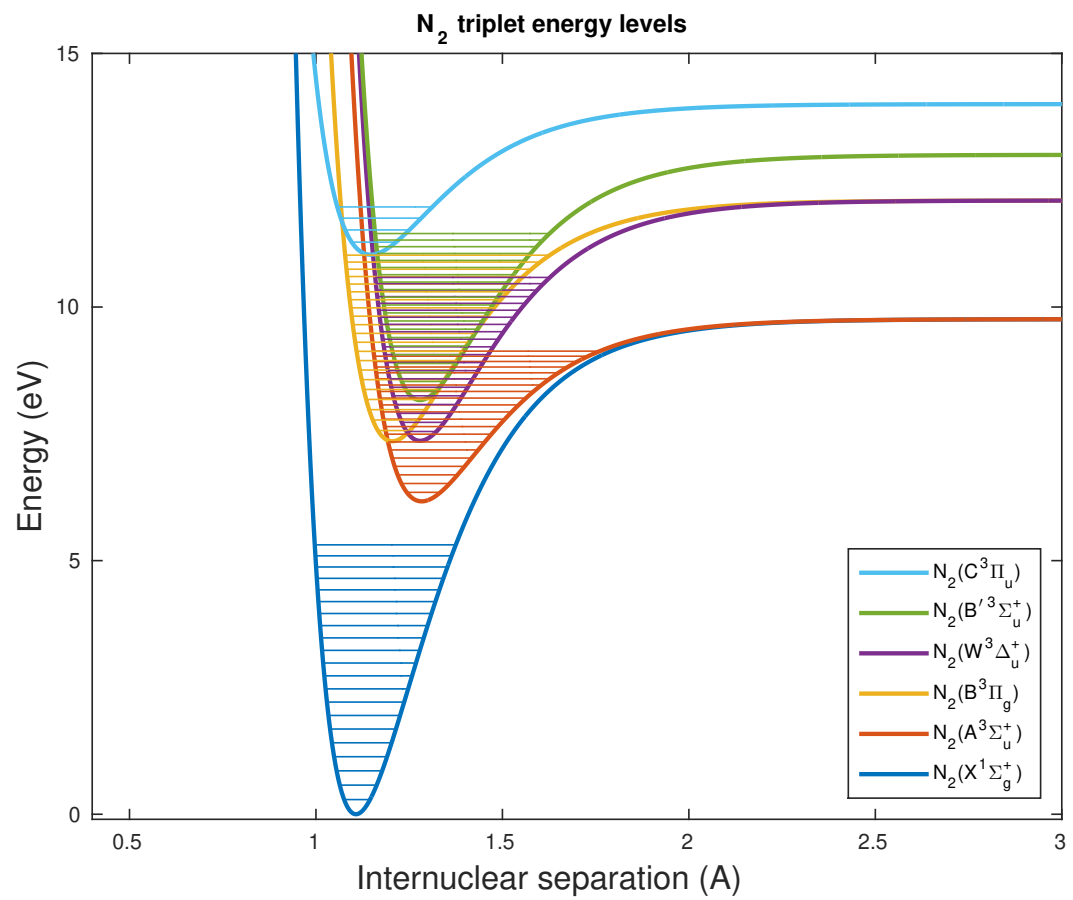


Figure 1.10: The energy-levels of the ground-state and the triplet-states of molecular nitrogen are plotted with the Morse-potential-curves illustrating how the vibrational states of the electronically excited states overlap.

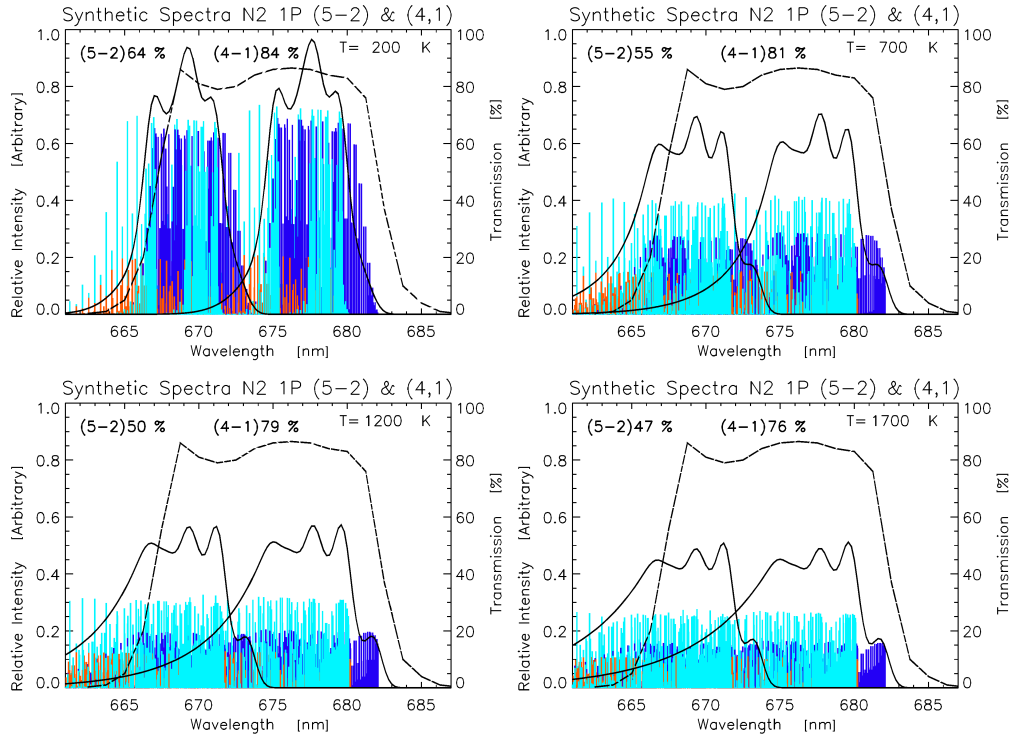


Figure 1.11: The distribution of the rotational transitions in the N₂ first positive 4-1 and 5-2 bands depends on the neutral temperature. From the upper-left to the bottom-right panel the spectra are calculated for neutral temperatures from 200 to 1700 K. Figure from Jokiah [2009].

Chapter 2

Electron transport

2.1 Electron impact Excitation

Auroral excitation is caused by electron-impact excitation. That is electrons with energy above the excitation threshold have some probability to excite the neutral particle. The excitation rate (in $m^{-3}s^{-1}$) is calculated by integrating the product of the excitation cross-section multiplied with the total electron flux (i.e. flux at energy E in all directions), multiplied with the density of the neutral species to be excited.

Similar to photo-ionization we get the electron (and proton) impact excitation due to all inelastic collisions of electrons with the neutral particles in a volume.

$$q_{n_j^*}(z) = n_j(z) \int_{E_{th}}^{\infty} I_e(E, z) \sigma_j^*(E) dE \quad (2.1)$$

where E_{th} and σ_j^* are the excitation-threshold and energy-dependent excitation-cross-section of the excited state n_j^* of the species n_j , and $I_e(E, z)$ is the total flux

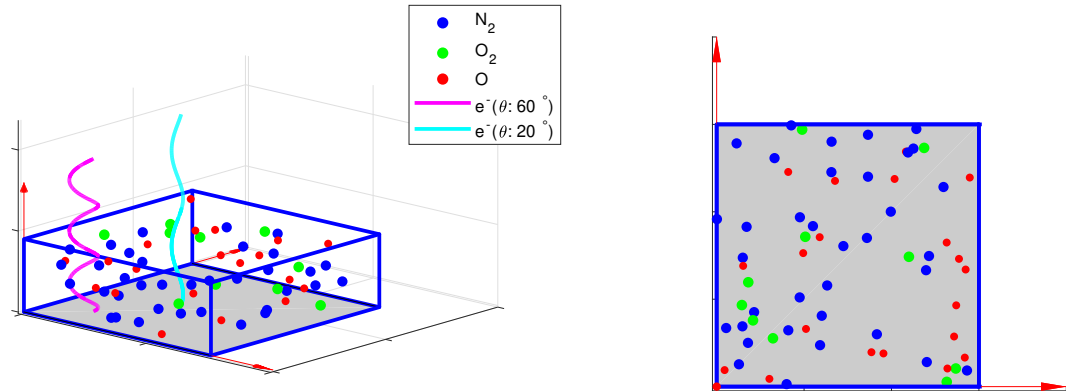


Figure 2.1: Illustration of total neutral-density cross-section and electron-trajectories.

Here the electrons' pitch-angles play the role of the solar-zenith-angle for the

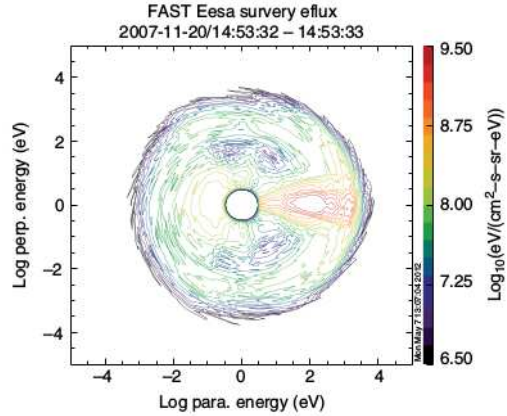


Figure 2.2: Pitch-angle-resolved electron energy-flux typical of Alfvénic precipitation with a predominantly field-aligned beam at energies below some 3 keV. From *Colpitts et al.* [2013].

path-length of the electron trajectory through an atmospheric layer.

2.2 Electron transport

To calculate the fluxes of electrons at thermospheric heights it is necessary to take into account all the processes that change the energy and direction of motion of energetic electrons spiraling down into the thermosphere from the magnetosphere along the earth's magnetic field. This can either be done with Monte Carlo modeling, where the trajectories of large numbers of electrons at the full energy-range of interest is traced taking into account the individual collisions and collecting the statistics of the particle flux. Or more simply solving the electron transport equations, i.e. the Boltzmann-equation multiplied with the velocity. At thermospheric altitudes the electron collisions with neutrals dominate the force-term in the Boltzmann equation and has to be included - while the force-term often can be simplified to only account for the magnetic mirror-force.

Electron transport, then, is “only” accounting for the change of electron-fluxes along a magnetic field-line. The practical calculations are challenging, but the underlying physics is simple, at least conceptually: an electron collides (or not), possibly loses some amount of energy, changes direction due to the collision (we only need to care about the change in pitch-angle). Possibly one or two secondary electrons are produced in ionizing collisions. The only thing necessary to do is to keep the accounting of these effects accurate for all energetic electrons along a magnetic field-line.

- The electron-impact collision-cross-sections varies with energy just as the photo-ionization cross-sections do.
- In collisions electrons can lose energy (inelastic collisions) or not (elastic collisions).

- They also change direction,
- and produce secondary electrons
- The magnetic mirror-force should also be accounted for.

2.2.1 Electron Collisions

Similar to photo-ionization we get the electron (and proton) impact excitation due to all the collisions of electrons with the neutral particles in a volume. However there is one major difference: photons vanish in ionization, electrons and protons do not.

Electron Collision Cross-sections

The electron-impact collision-cross-sections varies with energy just as the photo-ionization cross-sections do, see figure 2.1. The elastic collision cross-section dominates, at higher energies the ionization cross-section becomes close to equal. The inelastic cross-sections for O, O₂ and N₂ typically peaks between 5 and 25 eV, while the ionization cross-sections typically peaks between 50 and 200 eV. Further the total ionization-cross-sections are approximately 50 times larger than the sum of all the other inelastic cross-sections at energies above 100 eV. This has the consequence that primary electrons at energies above 1 keV predominantly cause ionization leading to production of secondary low-energy electrons that then collide inelastically and excite atoms and molecules. At low energies the vibrational cross-sections of molecular nitrogen are very large.

Collision-cross-sections are best estimated experimentally. Typical uncertainties are on the order of 10 per cent. The cross-sections presented here are extracted from compilations by *Itikawa and Ichimura* [1990], *Itikawa et al.* [1989] and *Itikawa et al.* [1986], the individual cross-sections have been measured experimentally in a number of laboratories over a long period of time and are known to typical accuracies on the order of 10% (see for example *Gronoff et al.* [2012]).

Angular scattering

In addition to the possible energy-loss electrons also change direction in collisions. The probability of electrons scattering by an angle, ψ when colliding with atoms and molecules have been measured. These scattering-probabilities varies with energy, but have been measured for atomic oxygen and molecular oxygen and nitrogen between a few eV and a few keV, separately for elastic, inelastic and ionizing collisions.

Scattering Measurements The measurements are done with instrumentation where a monoenergetic electron-beam is shot into a stream of dilute gas, then the number of electrons that are not colliding (and are propagating forward) and are colliding in a direction, ψ , are counted. This instrument was used to measure the

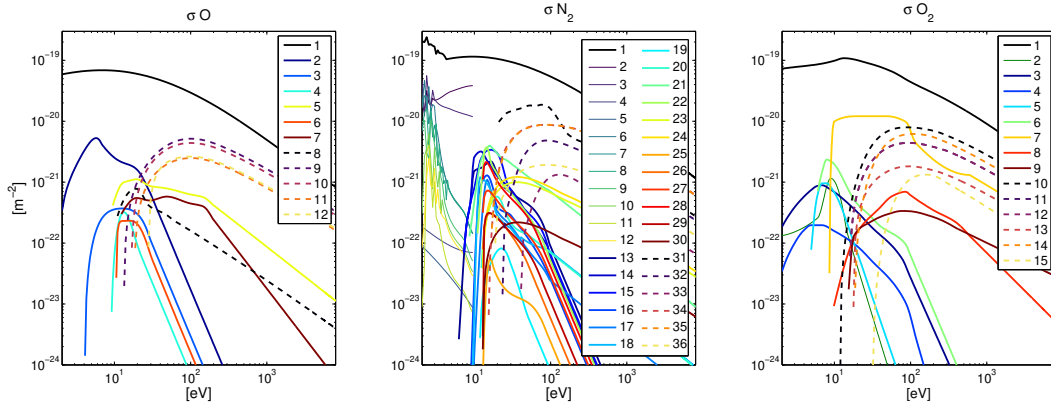


Figure 2.3: Electron collision cross-sections for atomic oxygen, molecular nitrogen and molecular oxygen are shown in the left, middle and right panels, respectively. The atomic oxygen cross sections are: 1 elastic, 2 $O(^1D)$, 3 $O(^1S)$, 4 $O(3s^3S_0)$, 5 $O(3s^3S_0)$, 6 $O(3p^5P)$, 7 $O(3s^3D_0)$, 8 $O(3p^3P)$, 9 $O^+(4S_0)$, 10 $O^+(2D_0)$, 11 $O^+(2P_0)$, 12 O^{++} . The molecular nitrogen cross sections are: 1 elastic, 2-5 rotational excitations 0-2, 0-4, 0-6 and 0-8, 6-12 vibrational excitations 0-1 to 0-7, 13 $N_2(A^3\Sigma_g^+)$, 14 $N_2(B^3\Pi_g)$, 15 $N_2(W^3\Delta_u)$, 16 $N_2(B^3\Sigma_u^-)$, 17 $N_2(a'^1\Sigma_u^-)$, 18 $N_2(w^1\Delta_u)$, 19 $N_2(E^3\Sigma_g^+)$, 20 $N_2(a''^1\Sigma_g^+)$, 21 $N_2(a^1\Pi_g)$, 22 $N_2(C^3\Pi_u)$, 23 $N_2(c'^1\Sigma_u^+)$, 24 $N_2(C^3\Pi_u)$, 25 $N_2(D^3\Sigma_u^+)$, 26 $N_2(F^3\Pi_u)$, 27 $N_2(G^3\Pi_u)$, 28 $N_2(M1M2)$, 29 $N_2(o^1\Pi_u)$, 30 dissociation, 31 $N + N^+$, 32 $N^+ + N^+$, 33 $N_2^+(X^2\Sigma_g^+)$, 34 $N_2^+(A^2\Pi_u)$, 35 $N_2^+(B^2\Sigma_u^+)$. The molecular oxygen cross-sections are: 1 elastic, 2 $O_2(\text{vib})$, 3 $O_2(a^1\Delta_g)$, 4 $O_2(b^1\Sigma_g^+)$, 5 4.5 eV, 6 6 eV, 7 8.4 eV, 8 9.97 eV, 9 $O_2(3S)$, 10 $O_2(X^2\Pi_g)$, 11 $O_2^+(a^4\Pi_u)$, 12 $O_2^+(16.9 \text{ eV})$, 13, $O_2^+(b^4\Sigma_g^-)$ 14, $O^+ + O$, 15, $O^+ + O^+$.

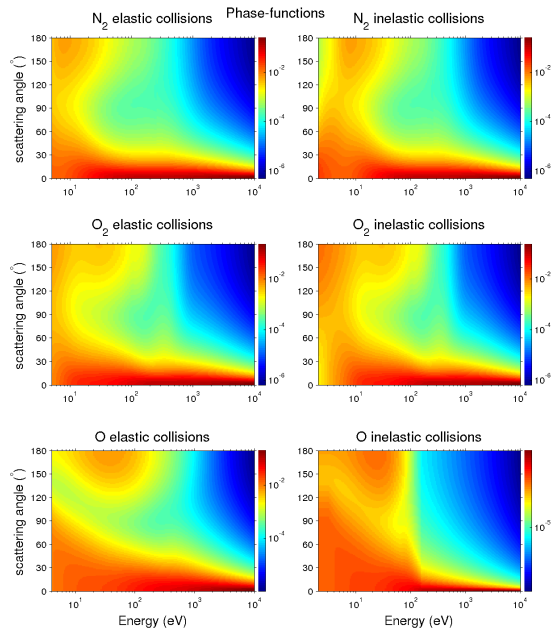


Figure 2.4: The phase-functions, for elastic (panels in left column) and inelastic (panels in the right column) for molecular nitrogen (top row), molecular oxygen (middle row) and atomic oxygen (bottom row) show the probability distribution for scattering-angles as a function of energy. Phase-function data from Sergienko, private communication.

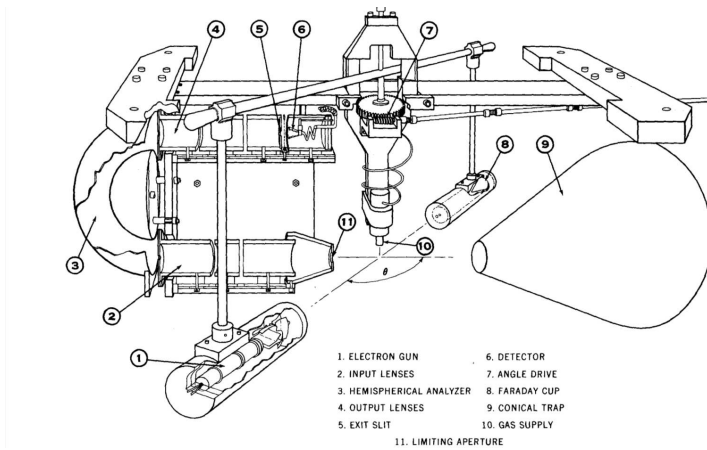


Figure 2.5: Measurements of electron-collision cross-sections are done in laboratories with instrumentation like this, from *Opal et al. [1972]*.

angular distribution of production of secondary electrons at diffent directions from the primary ionizing high-energy electrons.

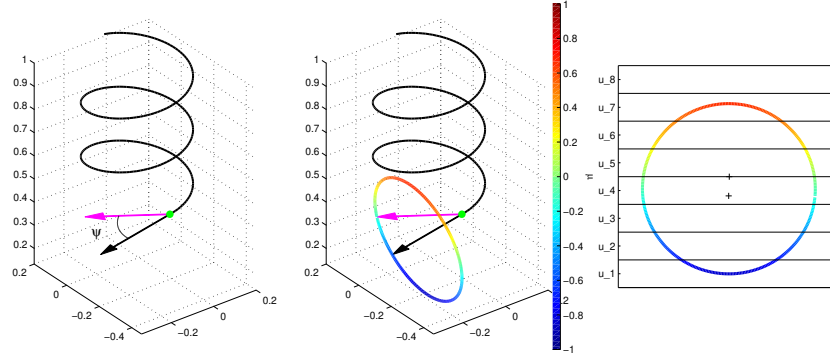


Figure 2.6: An electron colliding when propagating down along the magnetic field will scatter with some angle ψ , as shown in the left panel. Electrons scattering with angle ψ will have a uniform distribution over the clock-angle around the initial direction-of-motion, as shown in the middle panel, this will give those electrons new pitch-angles, marked with colour. As we use finite-sized pitch-angle-streams the contribution of electrons to each stream will be proportional to the fraction of the cone-of-propagation that falls inside the corresponding pitch-angle limits shown in the right panel.

The effect of angular scattering is to instantaneously change the direction of propagation of an electron. The “phase-functions” give us the probability-distribution of the scattering angle, ψ , in addition to that we need to take into account the fact that the probability distribution of the “azimuthal-scattering-angle” has a uniform distribution around the initial velocity, marked with the coloured circle in the middle panel. The change of importance for the electron-transport is the change in the field-aligned velocity component, i.e. the change in pitch-angle-cosine, since this changes the length of the electron-trajectory down into the thermosphere. The change of the velocity-components perpendicular to the magnetic field will lead to a shift of the gyro-centre, but this shift is small, on the order of an electron gyro-radius, and the widening of a pencil-beam of electrons is not more than a couple of gyro-radii, therefore this effect can typically be neglected.

Secondary-electron-spectra

In ionizing collisions the secondary electron are produced with some energy. The energy-distribution (spectra) of the secondary electrons produced by ionization of molecular nitrogen and oxygen are of the form:

$$P(E) \propto \frac{1}{\hat{E}^2 + E^2}$$

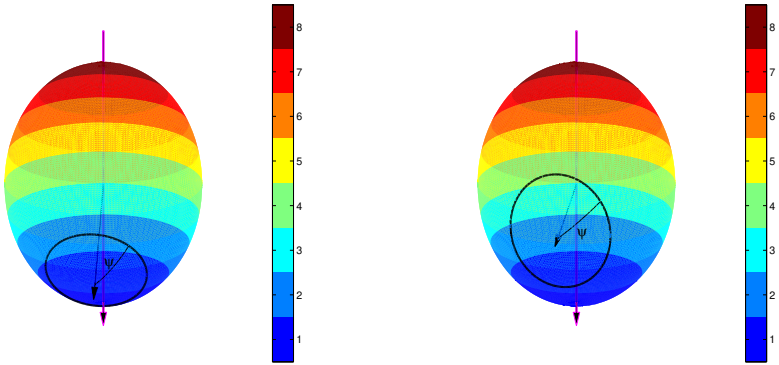


Figure 2.7: The change in direction-of-motion of electrons scattered with a scattering-angle, ψ , for two different initial pitch-angles, and the distribution of new direction-of-motion for the two cases. The coloured unit-sphere illustrates the pitch-angle-limits for an eight-stream configuration with uniform steps in μ_l from -1 to 1.

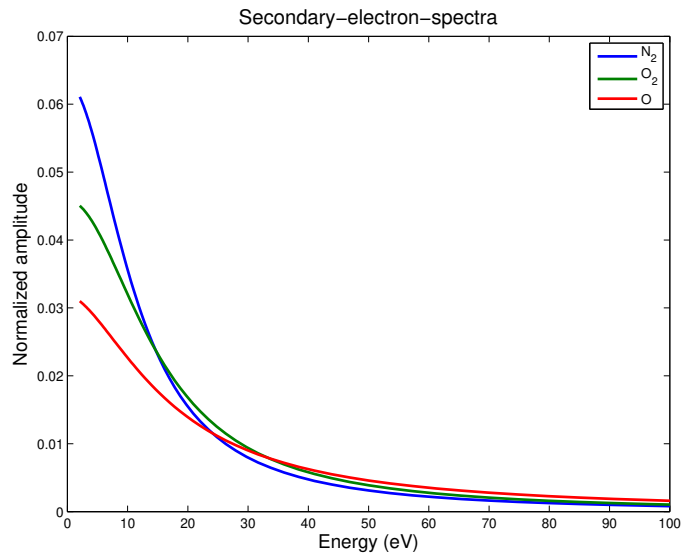


Figure 2.8: Energy-spectra of secondary electrons produced in electron-collisions with atomic oxygen and molecular oxygen and nitrogen are shown for energies between 0 and 100 eV.

where \hat{E} are 11.4 and 15.2 eV respectively. Secondary electrons produced in ionization of atomic oxygen have a similar energy-distribution:

$$P(E) \propto \frac{1}{1 + (E/A(E'))^{5/3}}$$

where $A(E)$ varies a bit with the energy, E' , of the ionizing primary electron. The production of secondary electrons is predominantly at energies below 20 eV, with a rather long higher-energy tail.

2.3 Electron Transport Calculations

2.3.1 Boltzmann Equation

More Rigorously we convert the Boltzmann equation:

$$\frac{\partial f}{\partial t} + \nabla_r \cdot (\mathbf{v}f) + \nabla_{\mathbf{v}} \cdot \left(\frac{\mathbf{F}}{m_e} f \right) = \frac{\delta f}{\delta t}_{coll} + \frac{\delta f}{\delta t}_{prod} + \frac{\delta f}{\delta t}_{loss}$$

by transforming from velocity components to kinetic energy, E , and unit direction vector, $\Omega = \mathbf{v}/|\mathbf{v}|$:

$$f(\mathbf{r}, \mathbf{v}, t) d^3 \mathbf{v} = \frac{v}{m_e} f(\mathbf{r}, E, \Omega, t) dE d^2 \Omega$$

Then we get the flux by multiplying the phase-space-density with the velocity:

$$I_e(\mathbf{r}, E, t) d^3 \mathbf{v} = \frac{v^2}{m_e} f(\mathbf{r}, E, \Omega, t)$$

The Boltzmann equation applies also to the phase-space-density of very high-energy particles. Since the electron-mobility is significantly smaller perpendicular to than along the magnetic field it is possible to use a one-dimensional Boltzmann equation. Further, since the energies of the primary electrons causing aurora, typically in the range from 100 eV to a few tens of keV, are several orders of magnitude larger than the thermal energy of the ionospheric electrons (with typical temperatures from 1000 to 3000 K, corresponding to thermal energies between 0.1 to 0.3 eV) the energetic electrons primarily interact with the ionosphere-thermosphere by collisions where no energy is ever gained. Therefore it is more convenient to convert the Boltzmann equation for phase-space-density to a transport equation for particle flux.

2.3.2 Transport equation

The transport of electrons (and similarly for protons) through our atmosphere can be described by the electron (proton-electron) transport equations:

$$\begin{aligned} \frac{1}{v(E)} \frac{\partial I(E, s, \mu, t)}{\partial t} + \mu \frac{\partial I}{\partial s} - \frac{1-\mu^2}{2B} \frac{\partial B}{\partial s} \frac{\partial I}{\partial \mu} &= - \sum_j n_j \sigma_j^{tot} I + \\ \sum_{j,\alpha} Q_{j,\alpha} + Q_{photo} - n_e \frac{\partial L_{ee}(E) I}{\partial E} \end{aligned} \tag{2.2}$$

When all other forces except the conservative magnetic mirror-force the transport equation is “only” a continuity-equation for electron-fluxes. While the Boltzmann equation coupled with the electromagnetic fields together with Maxwell’s equations describe the dynamic evolution of a plasma, the transport equations only describe the transport of electrons and are, bluntly put, only solving an accounting problem.

If the mirror-force can be neglected we arrive at the transport-equation on standard form:

The transport of electrons (and similarly for protons) through our atmosphere can be described by the electron (proton-electron) transport equations:

$$\begin{aligned} \frac{1}{v(E)} \frac{\partial I(E, s, \mu, t)}{\partial t} + \mu \frac{\partial I(E, s, \mu, t)}{\partial s} = & - A I(E, s, \mu, t) \\ & + B(E, s, \mu, t, I) \\ & + Q(E, s, \mu, t, I) \\ & + n_e \frac{\partial (L_{ee}(E) I(E, s, \mu, t))}{\partial E} \end{aligned} \quad (2.3)$$

2.3.3 Time-of-flight and steady-state

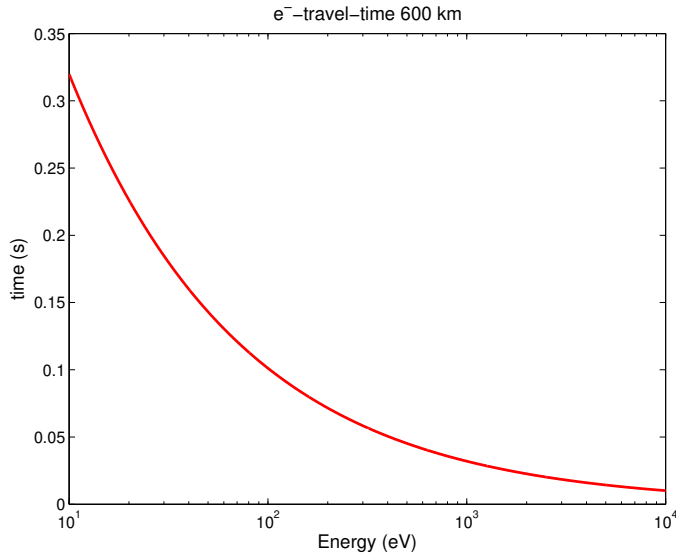


Figure 2.9: The field-aligned trans-ionospheric electron-time-of-flight varies with energy.

Since energetic electrons move with speed, their trans-ionospheric time-of-flight typically are much shorter than one second. For many cases where the electron-precipitation does not vary much on such short time-scales steady-state can be assumed to prevail.

This is not always the case, for example in flickering aurora where the intensity typically varies at frequencies between 5 and 15 Hz [Sakanoi and Fukunishi,

2004; *Whiter et al.*, 2010] the electron-fluxes will not reach steady-state and the full time-dependent electron-transport equations has to be solved [*Peticolas and Lumerzheim*, 2000]. As with all approximations made, one has to remember what constraints this introduces to the validity of ones solutions.

2.3.4 Steady-state Electron Transport Calculations

Considering the short travel-time we can make a steady-state approximation - typically the electron-precipitation does not vary too much on time-scales shorter than 0.5 s.

$$\begin{aligned} \mu \frac{\partial I(E, s, \mu)}{\partial s} = & - A I(E, s, \mu) + B(E, s, \mu, I) \\ & + Q(E, s, \mu, I) + n_e \frac{\partial (L_{ee}(E) I(E, s, \mu))}{\partial E} \end{aligned} \quad (2.4)$$

This is coupled differential equations, along s for electrons with all pitch-angle-cosines (μ) at energy E .

- Electrons do not gain energy - cascading down towards E_{th} .
- Not a PDE in (s, μ) since collisions spread electrons over full range of pitch-angles and not just to neighboring pitch-angles in a diffusion-type manner.

Multi-stream equations

The transport equations for electrons at energies above the smallest excitation threshold of interest in all pitch-angles are typically divided into difference-equations along s for electron-fluxes in a number of pitch-angle intervals (such that $I^j(E, s)$ is the electrons with pitch-angle-cosines between μ_j and μ_{j+1} and finite-sized energy-bins.

Since the electrons either dont lose energy (in elastic collisions) or lose energy (collisions leading to excitation, ionization, or “frictional” electron-electron collisions.) fluxes at higher energies do not depend on fluxes at lower energies. Therefore one can solve these equations starting from a highest energy and then proceed stepwise to lower energies.

The coupling between the different pitch-angle-streams are mathematically not a difference-type equation - since colliding electrons scatter from any pitch-angle to all other pitch-angles and not simlpy change pitch-angles gradually.

The first term on the right-hand side represents losses of electron flux from energy, E , and pitch angle-cosine, μ , due to elastic collisions changing the pitch angle and by inelastic collisions changing energy and possibly pitch-angle, with

$$A = \sum_k n_k(s) \sigma_k^{tot}(E)$$

The second term on the right-hand side represents elastic scattering of electrons from other pitch angles, μ' , to pitch angle μ :

$$B(E, s, \mu, t, I) = \sum_k n_k(s) \sigma_k^{el}(E) \cdot \int_{-1}^1 p_k^{el}(E, \mu' \rightarrow \mu) I(E, s, \mu', t) d\mu'$$

Here $p_k^{el}(E, \mu' \rightarrow \mu)$ is the probability that an electron with energy E and initial pitch-angle-cosine μ' will scatter to a pitch-angle-cosine μ .

In order to calculate the pitch-angle redistribution between the different streams the probability of scattering from one pitch-angle-stream to another has to be calculated. This is a geometric conversion from the angular scattering-probability-distribution to a pitch-angle-stream-to-pitch-angle-stream transfer factor.

The third term on the right-hand side, $Q(E, s, \mu, I)$, combines all internal sources of energetic electrons, i.e. production of photo-electrons and secondary electrons, and electrons cascading to energy E from higher energies, ε , due to inelastic collisions:

$$\begin{aligned} Q(E, s, \mu, I) = & \\ & Q_{local}(E, s, \mu) + \\ & \sum_{k,j} n_k(s) \sigma_k^j(\varepsilon \rightarrow E) \int_{-1}^1 p_k^j(\varepsilon, \mu' \rightarrow \mu) I(\varepsilon, s, \mu') d\mu' + \\ & \sum_k n_k(s) \int_{E+E^*}^{\infty} \sigma_k^{ion}(\varepsilon \rightarrow E) \int_{-1}^1 p_k^{ion}(\varepsilon, \mu' \rightarrow \mu) I(\varepsilon, s, \mu') d\mu' d\varepsilon \end{aligned} \quad (2.5)$$

Q_{local} is the local production of electrons - that is the sum of photo-electrons and secondary electrons. The summations in the second term are over all the excited states j of the k -th species. Electrons exciting an atom or a molecule lose a quanta of energy corresponding to the excitation energy, ΔE . Therefore electrons at energy ε that collide inelastically will contribute to the second term of Q at a series of discrete energies, $E = \varepsilon - \Delta E_k^j$ corresponding to the excitation thresholds of neutral species k . In ionizing collisions, represented with the third term in equation (2.5), the energy loss of primary electron is the sum of the ionization energy and the energy of the secondary electron.

Photo-electron production Photo-electrons produced in sun-lit parts of the thermosphere are also an internal source of energetic electrons, that should be included in these calculations. Typically the photo-electron production is taken as being completely isotropic, that is a photo-electron is equally likely to be produced in any direction. Photo-electrons can also be produced in the conjugate end of a magnetic field-line and propagate to our region of interest. These photo-electron-fluxes are, however, included in the primary electron-fluxes at the top of our ionosphere-thermosphere.

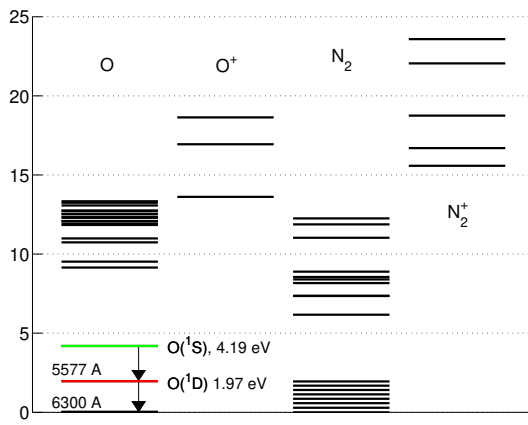


Figure 2.10: Energy-level diagram for atomic oxygen, atomic oxygen ions, molecular nitrogen and molecular nitrogen ions.

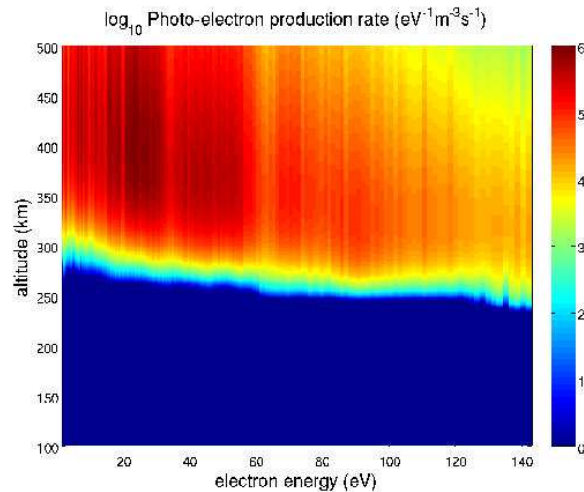


Figure 2.11: Photo-electron production in a partially sun-lit thermosphere-ionosphere with significant production at heights above 275 km.

Electron transport calculations: 2-stream

If we assume that the electron flux is nearly isotropic then it is possible to simplify to two electron streams:

$$\frac{1}{2} \frac{\partial I^u}{\partial s} = -AI^u(E, s) + BI^d(E, s) + n_e(s) \frac{\partial}{\partial E} [L(E)I^u(E, s)] + C(E, s) + Q(E, s)/2$$

$$-\frac{1}{2} \frac{\partial I^d}{\partial s} = -AI^d(E, s) + BI^u(E, s) + n_e(s) \frac{\partial}{\partial E} [L(E)I^d(E, s)] + C(E, s) + Q(E, s)/2$$

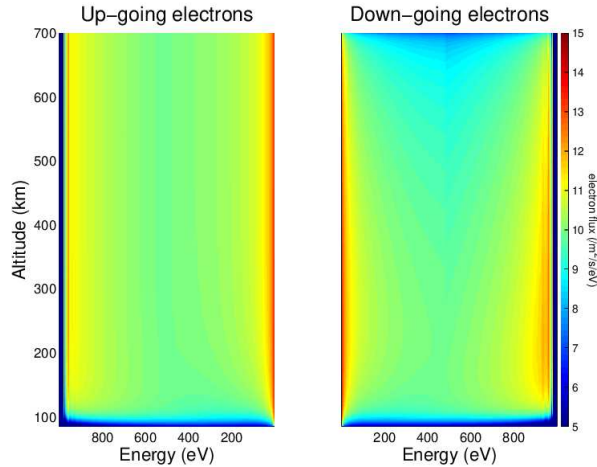


Figure 2.12: Electron-fluxes from a two-stream electron-transport code with 1 keV mono-energetic electron primary precipitation.

If we rewrite the 2-stream transport equation slightly (merging the Q and C terms and splitting the electron-electron term into A and the $C + Q$ term) we get the 2-stream transport equation on this form:

$$\frac{\partial}{\partial s} \begin{bmatrix} \bar{\mu}_u I^u \\ \bar{\mu}_d I^d \end{bmatrix} = \begin{bmatrix} -A' + B'_{uu} & B'_{du} \\ B'_{ud} & -A' + B'_{dd} \end{bmatrix} \begin{bmatrix} I^u \\ I^d \end{bmatrix} + \begin{bmatrix} QC^u \\ QC^d \end{bmatrix}$$

If we now refine the angular resolution to multiple pitch-angle-streams we can generalize the two-stream equation to a multi-stream electron-transport system:

$$\frac{\partial}{\partial s} \begin{bmatrix} \bar{\mu}_1 I^1 \\ \bar{\mu}_2 I^2 \\ \vdots \\ \bar{\mu}_n I^n \end{bmatrix} = \begin{bmatrix} -A' + B'_{11} & B'_{21} & \cdots & B'_{n1} \\ B'_{12} & -A' + B'_{22} & \cdots & B'_{n2} \\ \vdots & \vdots & \ddots & \vdots \\ B'_{1n} & B'_{2n} & \cdots & -A' + B'_{nn} \end{bmatrix} \begin{bmatrix} I^1 \\ I^2 \\ \vdots \\ I^n \end{bmatrix} + \begin{bmatrix} Q^1 \\ Q^2 \\ \vdots \\ Q^n \end{bmatrix}$$

Electron fluxes - 10-stream solution

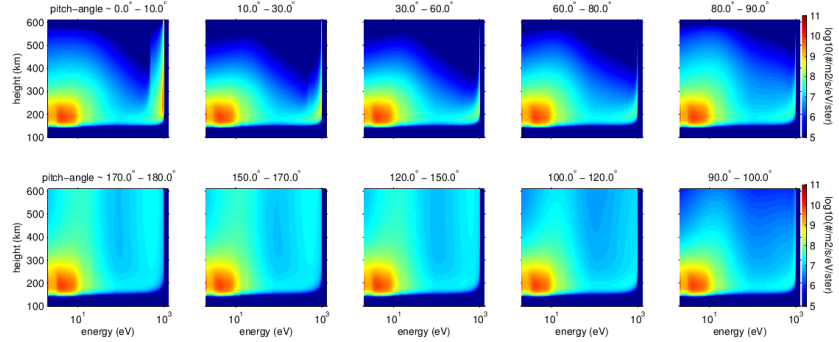


Figure 2.13: Electron-fluxes from a multi-stream electron-transport code with ten pitch-angle-streams run with isotropic 1 keV mono-energetic electron primary precipitation.

Electron fluxes omni-directional

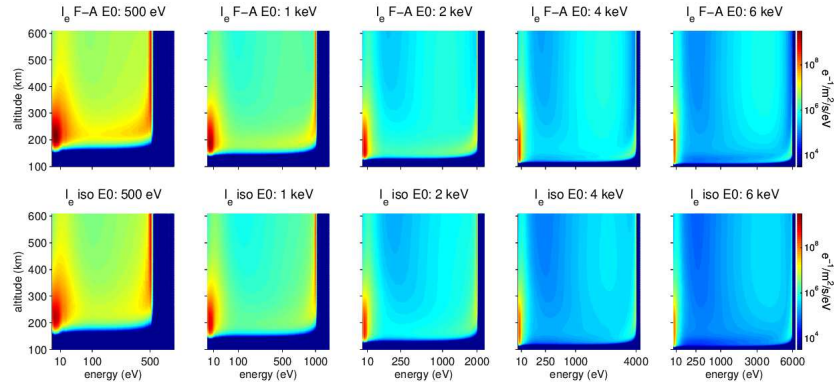
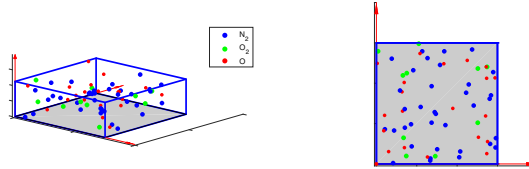


Figure 2.14: Omnidirectional electron-fluxes from a multi-stream electron-transport code with ten pitch-angle-streams run with mono-energetic electron primary precipitation with energies between 500 eV and 6 keV, with field-aligned pitch-angle distribution in the upper row of panels and isotropic pitch-angle-distribution in the bottom row of panels.



Electron impact Excitation

Now when the omnidirectional electron-fluxes are determined the electron impact excitation due to the collisions of electrons with the neutral particles can be calculated at all altitudes:

$$q_{n_j^*}(z) = n_j(z) \int_E^\infty I_e(E, z) \sigma_j^*(E) dE \quad (2.6)$$

Chapter 3

Aurora and Airglow - altitude and time-variations

3.1 Auroral Emissions I

The volume-emission-rate is proportional to the density of the excited species:

$$I_\lambda(\bar{r}) = A_\lambda^* n^*(\bar{r}) \quad (3.1)$$

Where A_λ^* is the Einstein coefficient for the transition from the excited state n^* that emits photons at wavelength λ . The density of the excited states we get from the continuity equation:

$$\frac{\partial n^*}{\partial t} + \mathbf{v} \cdot \nabla n^* + D \nabla^2 n^* = Q_{n^*}(\bar{r}, t) - \frac{n_{O1D}}{\tau_{n^*}} \quad (3.2)$$

Where D is the diffusion coefficient, and τ_{n^*} is the lifetime of n^* - taking all loss-processes into account.

A few points about the number-density of excited species and the continuity-equation: 1, atoms and molecules will convect with the neutral wind while ions typically are magnetized (above some 140 km) and will move with the ExB-drift in the F-region and parallel to the E-field in the lower E-region. These drifts doesn't have to be parallel, when the E-field changes it takes some time for the ions to change the neutral wind (due to the low ionization in the ionosphere). 2, depending on the lifetime, τ of the excited species drift and diffusion will have large or insignificant effect on the excited species density. Excited states with lifetimes on the order of micro-seconds and shorter, will not travel far before they emit the excess energy, excited states with lifetimes on the order of seconds and longer can move significantly from where they were produced.

3.2 Volume-Excitation-Rates

When we know the omni-directional (atoms and molecules are equally excited from any direction) electron-flux as a function of energy at all altitudes the excitation-rate

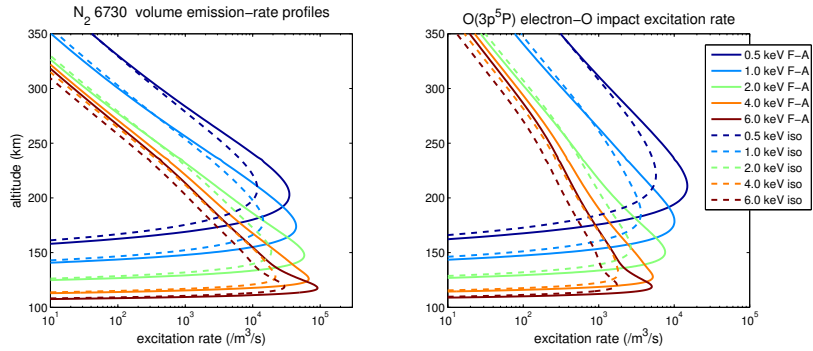


Figure 3.1: Volume emission-rate profiles of the 6730 and 7774 Å emissions produced by direct electron impact excitation of molecular nitrogen and atomic oxygen by mono-energetic electron-precipitation between 500 eV and 6 keV, show that the peak emission decreases with increasing energy, both for field-aligned and isotropic pitch-angle distribution of the primary electrons

can be calculated at every altitude according to equation (3.3).

$$q_{n_j^*}(z) = n_j(z) \int_E^\infty I_e(E, z) \sigma_j^*(E) dE \quad (3.3)$$

In figure 3.1 we see the volume excitation rates produced by monoenergetic electron-precipitation with constant total energy-flux for the states leading to emissions at 6370 Å (excitation of $N_2(B^3)$ leading to transition to $N_2(A^3)$, the “first positive band”) and 7774 Å (electron impact excitation of atomic oxygen to the $O(3p5P)$ state). We directly see a couple of things: that the altitude of peak excitation-rate of atomic oxygen are at a slightly higher altitude, that the fall-off above the excitation-peaks are shorter for the molecular nitrogen excitation (due to the smaller scale-height).

Most importantly we see that the peak volume excitation-rate of molecular nitrogen increases with increasing energy of the primary electrons, while it is decreasing for atomic oxygen excitation. The reason for this a short chain of arguments: the excitation of atoms and molecules are dominated by electrons with energies below 50 eV (check the collision-cross sections in figure 2.3), the peak production-rate of secondary electrons occur at lower and lower altitudes as the energy of the primary electrons increases, the mixing ratio of atomic oxygen ($n_O/(n_O + n_{O_2} + n_{N_2})$) decreases with decreasing altitude while the mixing-ratio of molecular nitrogen increases – so with increasing primary energy the production of secondary electrons occurs in an atmosphere with relatively more molecular nitrogen and less atomic oxygen - therefore the available energy of the secondary electrons will go to an increasing fraction go to excitation of molecular nitrogen and less and less will go to excitation of atomic oxygen.

Table 3.1: Excited state and radiative life-time for a few prominent auroral emissions.

| Excited-state | τ_R $1/\sum A_\lambda$ | Dominant Quenching | λ Å |
|----------------------|--------------------------------|--------------------|----------------|
| $O(^1D)$ | 107 s | N_2, O_2 | 6300, 6364 |
| $O(^1S)$ | 0.7 s | O_2, O | 5577, 2972 |
| $O^+(^2P)$ | 5 s | N_2 | 7319-7330 |
| $O^+(^2D)$ | 2.9 h | N_2 | 3727-3729 |
| $N_2(B^3\Sigma)$ | 6 μ s | N_2 | 6500-7500 |
| $N_2(A^3\Sigma_g^+)$ | 2 s | O | 1900-5600 |
| $N_2^+(A^2\pi)$ | 14 μ s | N_2 | 5500-IR |
| $N_2^+(B^2\Sigma)$ | 70 ns | N_2, O_2 | 3300-5800 |

3.3 Einstein coefficients and Lifetimes

To judge whether the convection and diffusion-terms are needed in the continuity equation we have to look at the radiative life-times, some of which are presented in table 3.1. For the $N_2(B^3\Sigma)$, $N_2^+(A^2\pi)$ and $N_2^+(B^2\Sigma)$ the lifetimes are so short that excited molecules and ions can not move far from where the excitation occurred, with a 100 m/s neutral wind the convection distance over a lifetime is on the order of $1 \cdot 10^{-3}$ m and smaller. The effect of this drift should be compared to the smallest typical scale-sizes in the aurora, where structures with horizontal sizes down to 50-100 m are seen. When the convection-diffusion-lengths are much smaller than the scale-size they will have a small effect on the distribution of the excited species, when they are on the same order of magnitude we should take them into account and if the convection-diffusion-distance are large compared to the horizontal scale-sizes they have to be accounted for, and . For $O^+(^2P)$ the E-cross-B-drift might become as large as a couple of km/s - and the convection-distance over a life-time might several kilometers. For the states with radiative life-times of 10s to 100s of seconds both drift and diffusion should be taken into account.

If the transport-terms in equation (3.2) can be ignored a simple first-order ordinary differential equation for the local number-density of n^* is obtained:

$$\frac{\partial n^*}{\partial t} = -n^*/\tau + q \quad (3.4)$$

The analytical solution to onset of constant excitation is

$$n^*(t) = q_0\tau \left(1 - e^{-t/\tau} \right) + n^*(0)e^{-t/\tau} \quad (3.5)$$

For radiative lifetimes on the order of 1 ns to a few 10 μ s the response-times to variations in excitation will not be resolved. Then, since steady-state conditions applies at all times we have:

$$n^*(t) = \tau q(t) \quad (3.6)$$

For the allowed transitions, i.e. from states with the very short lifetimes, the response-characteristics has such a short delay that it will be impossible to resolve

its effect in the aurora, therefore we can typically neglect it and use the steady-state condition.

With the persisting steady-state density of n^* we get the volume emission-rate at wavelength λ :

$$I_\lambda(t) = A_\lambda n^*(t) = A_\lambda \tau q(t) = \frac{A_\lambda}{\sum_{\lambda_i} A_{\lambda_i}} q(t)$$

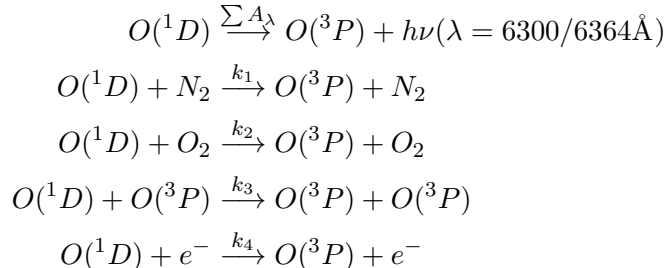
Where we can identify the $A_\lambda / \sum A_{\lambda_i}$ as the partitioning fraction of emissions from n^* at wavelength λ .

If we look at the last part of the equation above we see that the volume emission at wavelength λ is the $A_\lambda / \sum A_i$ -fraction of the total excitation-rate - that is when there are multiple possible transitions from an excited state the emission partitions according to their Einstein coefficients. From the $O(^1S)$ state there are transition to the $O(^1D)$ -state (emitting at 5577 Å) and to the atomic oxygen ground-state emitting at 2972 Å, see table 1.1. For an $O(^1S)$ excitation-rate of q_{1S} their volume emission-rates will be $A_{5577}/(A_{5577} + A_{2972})$ and $A_{2972}/(A_{5577} + A_{2972})$ respectively. (as long as we can ignore collisional de-excitation processes).

3.4 Forbidden Emissions

For the excited states with life-times that are long compared to the average time between collisions, like $O(^1D)$ $O(^S)$ and $O^+(^2P)$, collisions can lead to de-excitation. The excess energy goes to combinations of kinetic energy and excitation energy of internal states (primarily vibrational energy) of the colliding particles. In the literature this process is known as “quenching”. Since the collision-frequency depends on the density of colliding particles the rate of de-exciting collisions will vary with the neutral-density - and decrease with height. Below we will illustrate with the quenching of $O(^1D)$ $O(^S)$ and $O^+(^2P)$.

effective life-time – collisional loss-processes: $O(^1D)$ 6300 Å In addition to de-excitation by emitting photons $O(^1D)$ loses energy in collisions with nitrogen molecules, oxygen atoms and molecules and electrons. The respective reaction, are:



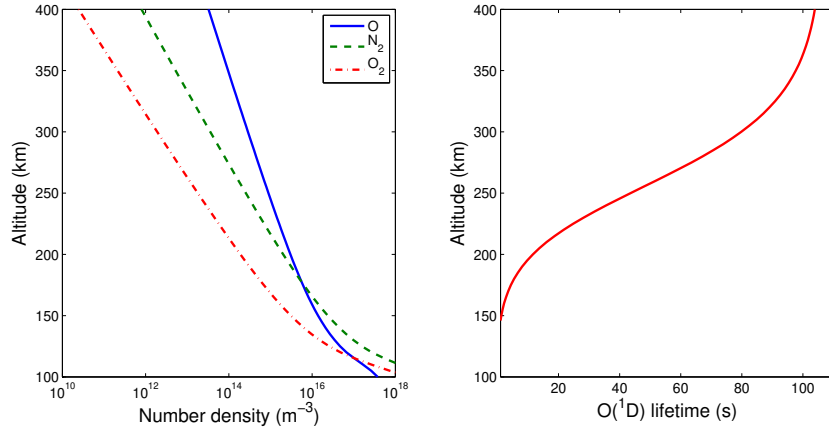


Figure 3.2: The thermospheric density-variation with altitude, shown in the left panel, makes the collisional quenching-rate depend on altitude which leads to the altitude-variation of the O(¹D) effective life-time shown in the right panel.

with the reaction-rates/quenching-rates:

$$\begin{aligned} k_1 &= 2.0 \cdot 10^{-11} \exp(107.8./T_n) \text{ (m}^3/\text{s)} \\ k_2 &= 2.9 \cdot 10^{-11} \exp(67.5./T_n) \text{ (m}^3/\text{s)} \\ k_3 &= 8 \cdot 10^{-12} \text{ (m}^3/\text{s)} \\ k_4 &= 1.6 \cdot 10^{-12} T_e^{0.91} \text{ (m}^3/\text{s)} \end{aligned}$$

The loss-term in the O(¹D) continuity equation can now be written:

$$\frac{n_{O1D}}{\tau_{O1D}} = (A_{6300} + A_{6364} + k_1 n_{N_2} + k_2 n_{O_2} + k_3 n_O + k_4 n_e) n_{O1D}$$

From which we can identify the effective life-time as the inverse of the sum of all “de-excitation-rates”:

$$\tau_{O1D}(z) = \frac{1}{A_{6300} + A_{6364} + k_1 n_{N_2} + k_2 n_{O_2} + k_3 n_O + k_4 n_e}$$

Since the densities of the colliding species and both the neutral and electron-temperatures all varies with altitude the collisional de-excitation-rate will vary with altitude, while the Einstein coefficients are constant. This gives us an altitude-varying effective life-time, a typical example are shown in the right panel of figure 3.2. Here it is worth pointing out that only at altitudes above 300 km the effective lifetime approaches the radiative life-time while at altitudes around 200 km (the typical altitude of the peak volume emission-rate at 6300 Å) the effective lifetime is some 30–40 s.

For O(¹S) and O⁺(²P) with shorter radiative life-times and slightly different quenching-rates the impact of quenching will happen at lower altitudes – where the exponentially higher neutral density will lead to rapid enough collisional de-excitation.

For the non-prompt transitions, i.e. those with longer radiative lifetimes than a few 10s of micro-seconds we typically have to account for drift, diffusion and growth and decay when integrating the continuity-equation of the excited species number density. Before doing that we first extend the simplified steady-state solution (equation 3.6) for the number-density of excited particles with long radiative lifetimes. This corresponds to the conditions after a period of constant production that is horizontally uniform over large enough region that drift and diffusion can be neglected. One example of this could be a wide stable auroral arc when drift and diffusion are not major factors for the near-IR emissions at 7320-7330 Å from $O^+(2P)$, since O^+ is magnetized at altitudes above 150 km. The effective life-time is however long enough to be of importance (and in general so is the drift at F-region altitudes where the ions will move with the E-cross-B-drift).

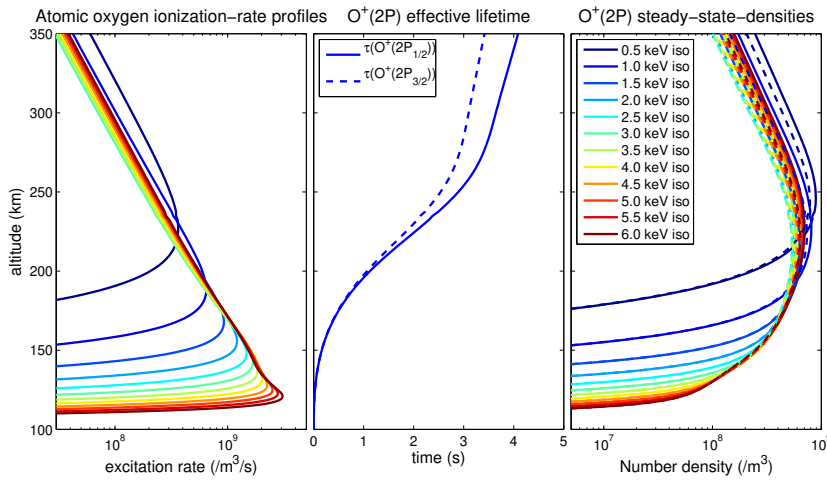


Figure 3.3: The altitude-profiles of the production, shown in the left panel, and the effective life-times, shown in the centre panel combine to produce the steady-state profiles of $O^+(2P)$ shown in the right panel.

Altitude-varying lifetimes: $O^+(2P)$ 7320-7330 Å The two $O^+(2P)$ states have radiative lifetimes of approximately 4.5 and 5.5 s, but some excited ions lose their energy in collisions with oxygen atoms and nitrogen molecules, this shortens the life-time of the excited ions at lower altitudes. If we take the altitude-variation of the effective life-time into account in equation (3.6) the steady-state density of $O^+(2P)$ will be:

$$n_{O^+(2P)}(z) = \tau(z)q_{O^+(2P)}(z)$$

and since the life-time decreases rapidly towards lower altitudes the steady-state altitude-profiles (shown in the right panel of figure 3.3) of $O^+(2P)$ are shifted towards higher altitude and varies much less than the ionization/excitation/production-profiles.

Here we have taken ionization-profiles from mono-energetic electron-precipitation (in the left panel above, ionization-profiles from monoenergetic electron-precipitation (E_0 between 500 eV and 6 keV) with constant number-flux, i.e. increasing total energy-flux), but even though the total production of $O^+(2P)$ are significantly larger for the higher-energy precipitation it is predominantly at altitudes where the collisional de-excitation is dominating and the effective life-time is short.

Time-response When the excitation varies on time-scales comparable to the effective life-time it is necessary to take the time-variation of the excited state into account. This is typically the case for the forbidden states in normal auroral situations.

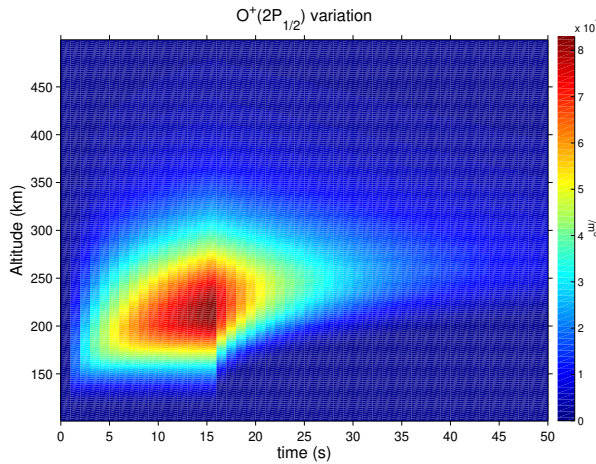


Figure 3.4: The time-altitude response of $O^+(2P)$ number-density to a pulse of 2 keV precipitation with 150 s duration display the time-respons-variation with altitude.

For the simplest case with an on-off pulse of precipitation leading to a constant excitation-rate at each altitude during the on-phase the time-response of the $O^+(2P)$ is at each altitude on the form:

$$n_{O^+(2P)}(t, z) = \tau(z) q_{O^+(2P)}(z) (1 - e^{-t/\tau(z)})$$

during the period with ionization. This should be recognized in figure 3.4 above as the rapid growth to a steady-state density at altitudes below 150 km, where τ is on the order of a second or shorter, and an increasingly more extended growth at higher altitudes, where steady-state is not really reached at altitudes above 200 km during the 15 s period with precipitation. For the period after ionization, $t > 15$ s, the $O^+(2P)$ density decreases as

$$n_{O^+(2P)}(t, z) = n_{O^+(2P)}(15, z) e^{-(t-15)/\tau(z)}$$

This is seen as the exponential decay after 15 s where the $O^+(2P)$ density decreases slower at higher altitudes where τ approaches the radiative life-time.

For the case where we have to take drift of the excited particles into account, which typically is necessary for $O^+(^2P)$ which moves with the ion-drift that can be significant on 10 s timescale compared to the spatial structure in the auroral precipitation, the expression for the excited number-density becomes

$$n_{O^+(^2P)}(\mathbf{r}, t) = \int_{-\infty}^t \exp\left(-\frac{t-\tilde{t}}{\tau_z}\right) \cdot q_{O^+(^2P)}\left(\mathbf{r} - \int_{\tilde{t}}^t \mathbf{v}_i(\mathbf{r}, t') dt', \tilde{t}\right) d\tilde{t} \quad (3.7)$$

In principal this is not a difficult equation to integrate, in practise, however, it is typically difficult to estimate both the spatially and time-varying $O^+(^2P)$ production rate $q_{O^+(^2P)}$ and the ion-drift velocity \mathbf{v} . In the second factor above it is easiest to identify drift-effect of excited particles if the drift-velocity \mathbf{v} is constant in both space and time, then $q_{O^+(^2P)}(\mathbf{r} - \mathbf{v}_i(t-\tilde{t}), \tilde{t})$ – that is at time t the production at an earlier time \tilde{t} has moved $\mathbf{v}_i(t-\tilde{t})$. $-\infty$ can typically be set at some 5 times the radiative life-time, production at earlier times have by and large decayed down to back-ground levels. That we can ignore the effects of diffusion for excited ions is because they are magnetized and gyrating around the magnetic field in the horizontal direction.

For excited neutral particles, such as $O(^1D)$, diffusion also has to be accounted for. Diffusion can be modeled as a convolution with a Gaussian kernel which leads to the formal equation for the excited number-densities:

$$\begin{aligned} n(\mathbf{r}, t) &= \int_{-\infty}^t \exp\left(-\frac{(t-\tilde{t})}{\tau_z}\right) \cdot q_{O(^1D)}\left(\mathbf{r} - \int_{\tilde{t}}^t \mathbf{v}(t') dt', \tilde{t}\right) \\ &\otimes \left(\frac{\pi^{-3/2}}{[\int_{\tilde{t}}^t D(t') dt']^{1.5}} \exp\left(\frac{-|\mathbf{r}|^2}{\int_{\tilde{t}}^t D(t') dt'}\right) \right) d\tilde{t} \end{aligned} \quad (3.8)$$

Here too the problem is determining $q_{O(^1D)}$ the time-varying three-dimensional production of $O(^1D)$, while the evaluation of equation (3.8) is “not difficult” once $q_{O(^1D)}(\mathbf{r}, t)$ is given.

3.5 Column-Emission-Rates

It is not possible to directly observe volume-emission-rates, what we observe with optical instrumentation is column-emission-rates, as illustrated in figure 3.5. Pixel in a camera adds photons emitted from within the field-of-view of the pixel, i.e. integration of the volume emission-rate along the line-of-sight. Due to the line-of-sight integration there is no range-resolution. However by combining observations from multiple sites it is possible to use stereoscopic triangulation and tomographic inversion-techniques to retrieve some of the three-dimensional variation of the volume emission-rates, see for example *Gustavsson* [2000] or *Semeter* [1997] for details. One can combine column-emission-rates from multiple emissions to extract information about the energy of the primary electrons, see for example *Rees and Luckey* [1974], *Strickland et al.* [1989], *Meier et al.* [1989], *Hecht et al.* [1989] or *Rees and*

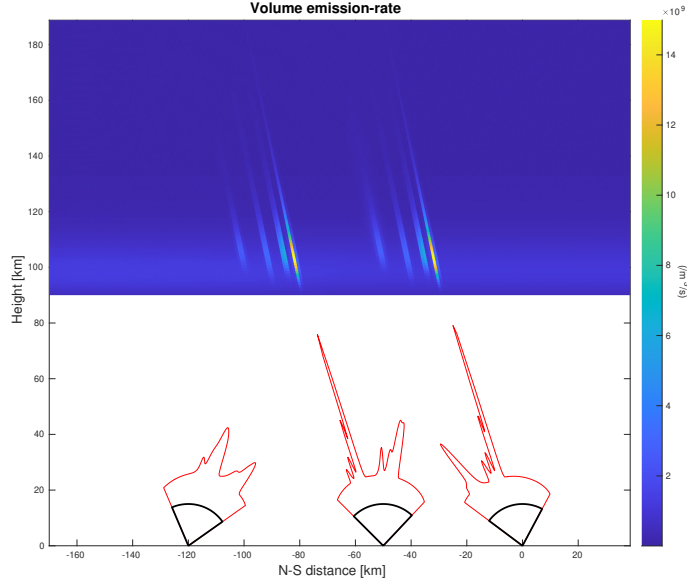


Figure 3.5: Illustration of how fine-scale structures in aurora can only be resolved when observed close to magnetic zenith.

Lummerzheim [1989], this is because emissions from atomic oxygen and molecular nitrogen responds differently to precipitation with increasing energy. Preferably both methods should be combined, ideally with incoherent scatter-radar observations of the time-variation of the electron-density-profiles, see for example *Tuttle et al.* [2014].

Altitude Variations: Ionization

3.6 Ionization-profiles

The same line of reasoning holds for the ionizing collisions, i.e. ionization-rate of atomic oxygen has a larger scale-height above the altitude of peak ionization than the molecular ionization-rates, the altitude of peak ionization-rate gets lower as the energy of the primary electrons increases. However we typically cannot observe the separate altitude-profiles of the ionization-rates. However, with incoherent scatter radars it is possible to observe the time-variation of the electron-density profiles, and since the electron density follows the electron continuity equation (E-region version):

$$\frac{\partial n_e(t, z)}{\partial t} = -\alpha_{avg} n_e(t, z)^2 + q_e(t, z)$$

we can obtain an indirect measure of the ionization-profiles:

$$q_e(t, z) = \alpha_{avg} n_e(t, z)^2 + \frac{\partial n_e(t, z)}{\partial t}$$

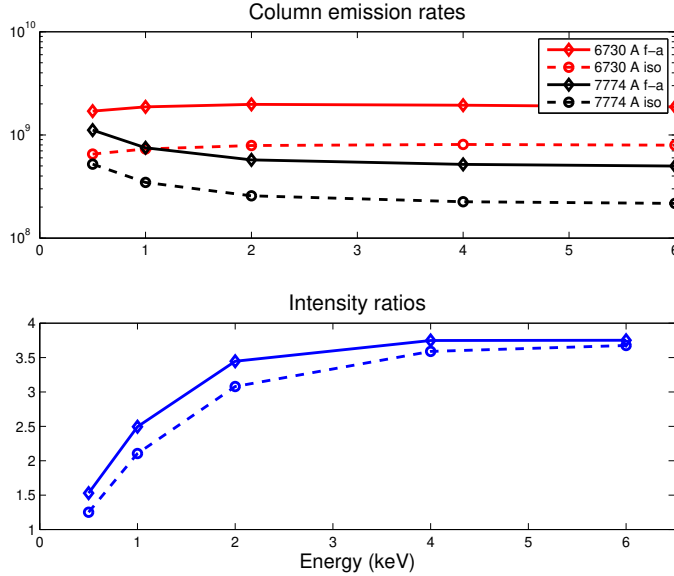


Figure 3.6: The column-emission-rates of the 6730 and 7774 Åemissions have opposite response to variation of the energy of mono-energetic precipitation. The N₂-emission increases while the O-emission decreases with increasing energy.

Altitude Variations: Ionization Since the electron-transport equations are linear differential equations the superposition-principle applies. Therefore we can write the total ionization profile as a sum of ionization-profiles caused by mono-energetic electron-fluxes:

$$\begin{aligned}
q(z_{top}, t) &= Q_1(z_{top})I_p(E_1, t) + Q_2(z_{top})I_p(E_2, t) + \cdots + Q_n(z_{top})I_p(E_n, t) \\
&\vdots \\
q(z_1, t) &= Q_1(z_2)I_p(E_1, t) + Q_2(z_2)I_p(E_2, t) + \cdots + Q_n(z_2)I_p(E_n, t) \\
q(z_1, t) &= Q_1(z_1)I_p(E_1, t) + Q_2(z_1)I_p(E_2, t) + \cdots + Q_n(z_1)I_p(E_n, t)
\end{aligned}$$

Here $Q_i(z)$ is the ionization rate produced at altitude z by a unit primary electron-flux I_p at energy E_i , i.e. a point on the ionization-profiles in the figure.

We can rewrite these equations on matrix form with the left-hand size being the ionization-profile and the right-hand side as a matrix-vector product between the primary electron-spectra as an array with electron-fluxes at a number of discrete energy-intervalls and a ionization-profiles-matrix:

$$\mathbf{q}_z = \mathbf{Q}_{E2z} \cdot \mathbf{I}_p(E)$$

This we can combine with the electron-density-based estimate of the ionization-rates to give us a system of equations that can be used to estimate the energy-spectra of the primary electrons causing the time-variation of electron-densities:

$$\mathbf{q}_z = \alpha_{avg} \mathbf{n}_e(t, z)^2 + \frac{\partial \mathbf{n}_e(t, z)}{\partial t} = \mathbf{Q}_{E2z} \cdot \mathbf{I}_p(E)$$

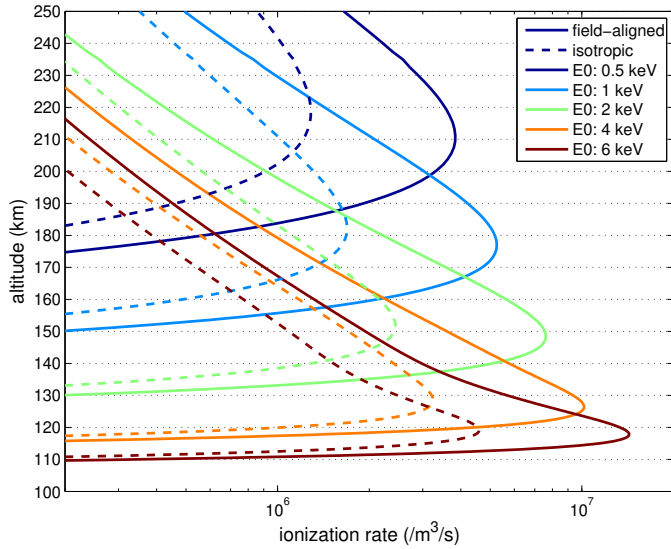


Figure 3.7: The ionization-profiles varies with energy of the primary electrons.

3.6.1 Estimate of Primary Electron-spectra

This gives us an estimate of the primary electron spectra:

$$\mathbf{I}_p(E) = \mathbf{Q}_{\mathbf{E}2z}^{-1} \cdot (\alpha_{avg} \mathbf{n}_e(t, z)^2 + \frac{\partial \mathbf{n}_e(t, z)}{\partial t})$$

There are two practical problems with this estimate, the first is that explicitly calculating the time-derivative of the electron-densities is a noise-amplifying operation (remember the lab-physics course.) and the matrix with monoenergetic ionization-profiles $\mathbf{Q}_{\mathbf{E}2z}$ is ill-conditioned (is close to “not full rank”), however more robust methods have been developed to handle these problems.

3.7 Monoenergetic spectra

The reason we look at the excitation and ionization-profiles resulting from monoenergetic precipitation is that any electron energy-spectra can be approximated by a sum of mono-energetic spectra - similar to a Riemann-sum for evaluating an integral. This works since the electron-transport-equation is a linear equation - hence the superposition-principle applies. In practice the electron-transport-equation is solved with electron-fluxes in narrow energy-bins. For the matlab-code in the computational exercise the width in energy varied from 0.17 eV below 10 eV, to 12 eV from about 100 eV and above.

3.7.1 Typical electron-energy-spectra

When calculating typical ionospheric responses an often used type of electron spectra is isotropic in pitch-angle with a Maxwellian high-energy component with a

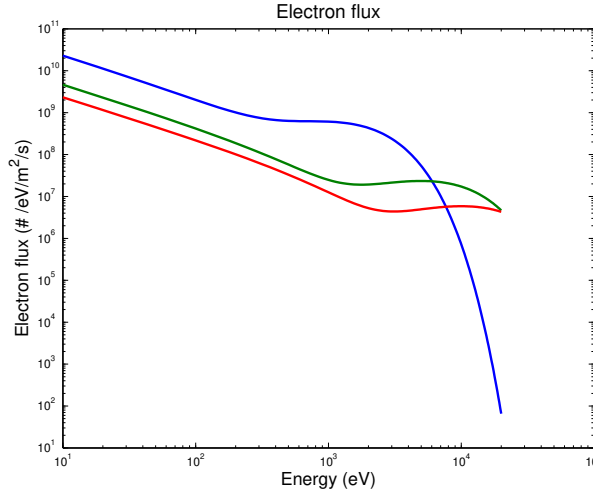


Figure 3.8: Electron-spectra example typical for discrete aurora, composed of Maxwellian-type high-energy component with energies of 2.5 and 10 keV and power-law-like low-energy-tails.

power-law low-energy tail. This type of electron-precipitation is rather common for precipitation in stable auroral-arc situations, and are the result of electro-static potential-drops accelerating magnetospheric electrons down into the ionosphere and reflecting upstreaming low-energy electrons back down. A typical spectra is the Maxwellian spectra:

$$I_e(E) = \frac{Q}{2\pi E_0^3} E \exp(-E/E_0) + \frac{Q}{5E_0 E \pi} \exp(-\frac{E}{b} - 1) \text{ (/eV/m}^2/\text{s/ster)}$$

where E_0 (eV) is the peak-energy, Q (eV/m²/s) is the total energy-flux and $b = E_0/10 + 350$. Above are electron-spectra for E_0 of 1.5 and 10 keV.

Correspondnig ionization-profiles

3.8 Ionization profiles for the “typical” spectra

Above are the total and atomic oxygen ionization profiles, plotted with dashed lines and thick solid lines respectively.

Combining time-n-alitude-variations Let us look at the 7320-7330 Å doublet

$$I_{7320}(\bar{r}) = A_{7320}^{1/2} n_{O^+(2P_{1/2})}(\bar{r}) + A_{7320}^{3/2} n_{O^+(2P_{3/2})}(\bar{r})$$

$$\frac{\partial n_{O^+2P}}{\partial t} + \mathbf{v}_{ExB} \cdot \nabla n_{O^+2P} + D \nabla^2 n_{O^+2P} = Q_{O^+2P}(\bar{r}, t) - \frac{n_{O^+2P}}{\tau_{O^+2P}}$$

Since O^+2P is magnetized diffusion will be small at F-region altitudes.

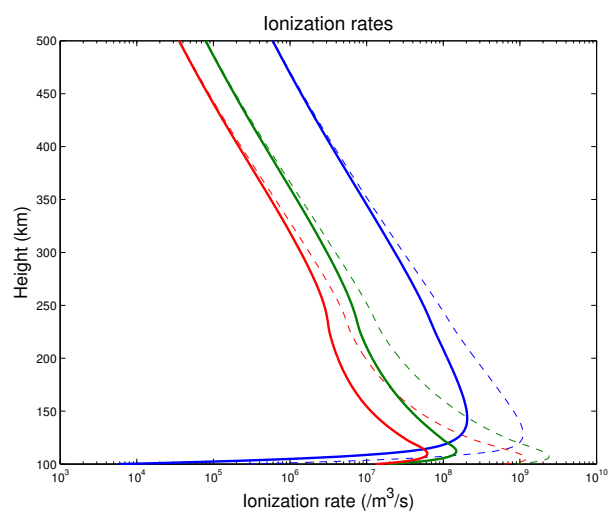


Figure 3.9: The ionization-profiles produced by the electron-spectra presented in figure 3.8.

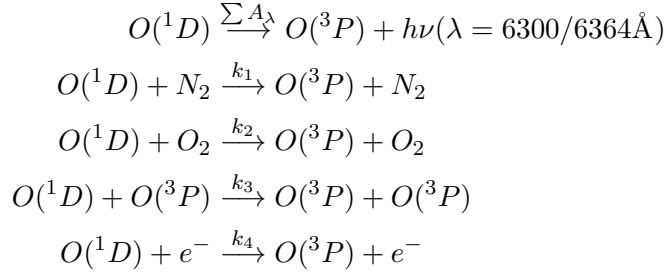
3.9 Auroral Red Line

$$I_{6300}(\bar{r}) = A_{6300} n_{O1D}(\bar{r})$$

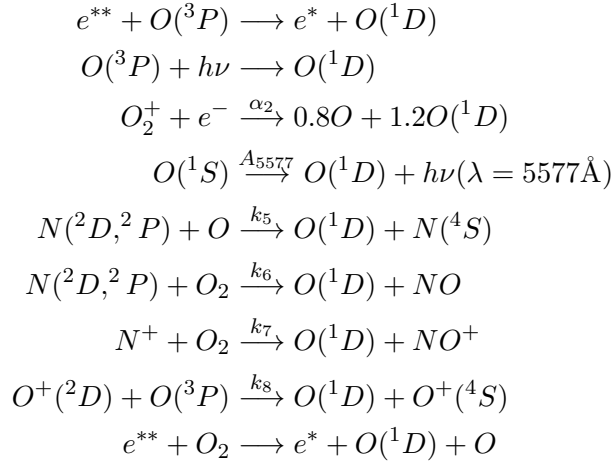
$$\frac{\partial n_{O1D}}{\partial t} + \mathbf{v}_n \cdot \nabla n_{O1D} + D \nabla^2 n_{O1D} = Q_{O1D}(\bar{r}, t) - \frac{n_{O1D}}{\tau_{O1D}}$$

The prominent 6300 Å “auroral red line” emitted by atomic oxygen in the $O(^1D)$ state is also a forbidden transition, the radiative life-time of $O(^1D)$ is 107 s. Just as for $O^+(2P)$ all terms in the continuity-equation should be accounted for, also diffusion, the drift now will be due to the neutral wind. Except these changes everything is similar when it comes to the integration of the continuity-equation. The main difference is that the effective life-time becomes longer and therefore the response-times correspondingly longer.

$O(^1D)$ 6300 Å: Sinks



$O(^1D)$ 6300 Å: Sources



3.10 Production of $O(^1D)$

Since the excitation-threshold of $O(^1D)$ is only 1.96 eV a number of chemical reaction in the thermosphere-ionosphere are exothermic enough to release enough energy to

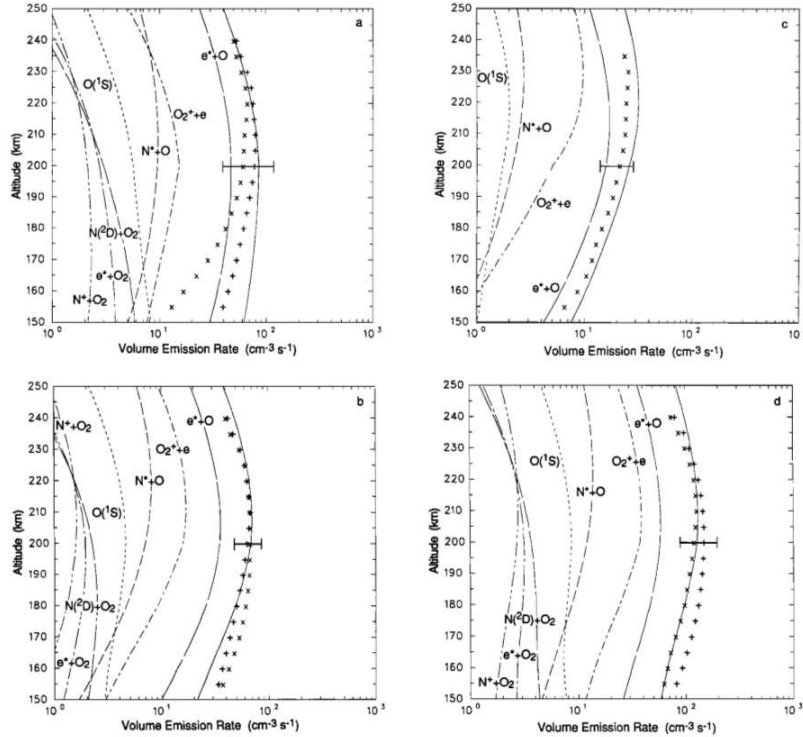


Figure 3.10: Modeled and measured 6300 Å volume emission rates plotted as a function of altitude. (a) AE-C orbit 5376 from 34100 to 34190 s UT. (b) AE-C orbit 5378 from 44890 to 44990 s UT. (c) AE-C orbit 5631 from 15760 to 15860 s UT. (d) AE-C orbit 6136 from 40650 to 40740 s UT. Solid line, total modeled; broken line, $e^* + O$; dash-dot, $O_2^+ + e$; short dashes, $N^* + O$; long dashes, $N(2D) + O_2$; dotted line, $O(^1S)$; long dash-dot, $e^* + O_2$; dash-dot-dot, $N^+ + O_2$; plus, measurement in forward direction; cross, measurement in backward direction. The error bar represents the estimated uncertainty in the measured profile. From *Solomon et al. [1988]*.

excite oxygen atoms - if they are produced by the reaction.

$O(^1D)$ 6300 Å: Sources

3.11 Production of $O(^1D)$

The dominant sources of $O(^1D)$ in aurora are direct electron-impact excitation of atomic oxygen and dissociative recombination of molecular oxygen ions. Then there are the full list of minor sources shown in the figure above.

Forbidden Emissions: $O(^1D)$ 6300 Å

$$I_{6300}(\bar{r}) = A_{6300} n_{O1D}(\bar{r})$$

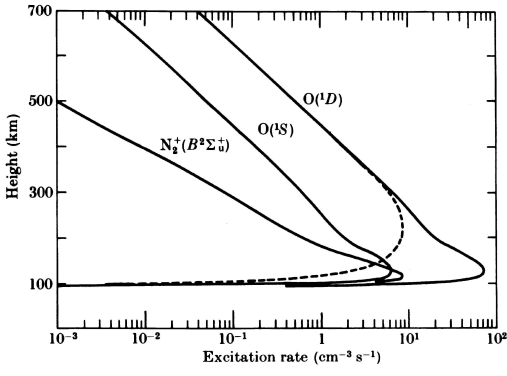


Figure 3.11: QUE-FIG

$$\frac{\partial n_{O1D}}{\partial t} + \mathbf{v} \cdot \nabla n_{O1D} + D \nabla^2 n_{O1D} = Q_{O1D}(\bar{r}, t) - \frac{n_{O1D}}{\tau_{O1D}}$$

3.12 Altitude-profiles of 6300 Å volume-emission-rates

Even though $O(^1D)$ has the largest volume excitation-rate (high excitation-cross-section combined with a low excitation-threshold that allows the secondary electrons with energies down to 1.96 eV to excite.) it is not the dominant emission at altitudes below 150 km – due to the collisional quenching.

3.13 Time-variation of $O(^1S)$ and the 5577 Å emission

With a 0.7 s radiative lifetime we can (typically) neglect drift and diffusion for $O(^1S)$, which simplifies the continuity equation to:

$$\frac{\partial n^*(t)}{\partial t} = -n^*(t)/\tau + q(t)$$

This we can solve:

$$\begin{aligned} \frac{\partial n^*(t)}{\partial t} &= -n^*(t)/\tau + q(t) \Rightarrow \\ \left\{ n(t) = \eta(t)e^{-t/\tau} \Rightarrow \frac{\partial n^*(t)}{\partial t} = \frac{\partial \eta(t)}{\partial t}e^{-t/\tau} - \frac{\eta(t)e^{-t/\tau}}{\tau} \right. \\ \frac{\partial \eta(t)}{\partial t}e^{-t/\tau} - \frac{\eta(t)e^{-t/\tau}}{\tau} &= \frac{\eta(t)e^{-t/\tau}}{\tau} + q(t) \Rightarrow \\ \eta(t) &= \int_{t_0}^t q(t')e^{t'/\tau} dt' \Bigg\} \Rightarrow \\ n(t) &= e^{-t/\tau} \left(\int_{t_0}^t q(t')e^{t'/\tau} dt' + n(t_0) \right) \end{aligned}$$

For the states with life-times shorter than 2 s drift and diffusion does not have too large effects on the local density of the excited species, however if the time-variation of the electron-precipitation varies at shorter time-scales than that the life-time of the excited state has to be taken into account when calculating the time-variation of the volume-emission-rates. Fortunately when the drift and diffusion-terms are simplified away from the continuity-equation it becomes an ordinary linear differential equation at each altitude. These equations we can trivially integrate at each altitude to obtain altitude-profiles of $O(^1S)$.

$$\frac{\partial n^*(t)}{\partial t} = -\frac{n^*(t)}{\tau} + q(t)$$

has a response to onset of constant excitation starting at time $t = 0$:

$$n^*(t) = q\tau(1 - \exp(-t/\tau))$$

$$\frac{\partial n^*(t)}{\partial t} = -\frac{n^*(t)}{\tau} + q(t)$$

With a harmonically varying excitation starting at time $t = 0$:

$$\frac{\partial n^*}{\partial t} = -\frac{n^*(t)}{\tau} + \frac{q}{2}(1 - \cos(\omega t))$$

we get (for $\omega > 0$):

$$n^*(t) = \frac{q\tau(1 - \cos(t\omega) - \tau\omega \sin(t\omega))}{2(\tau^2\omega^2 + 1)} + \frac{q\tau^3\omega^2}{2\tau^2\omega^2 + 2}(1 - e^{-\frac{t}{\tau}})$$

Harmonic response Since the transport-less continuity equation is a first-order linear ODE with constant coefficient we can study its behaviour by looking at its impulse-response or look at the response to a harmonic excitation. Here we look at the harmonic response - this is because there are auroras with almost harmonic intensity variation at frequencies up to 15 Hz (Flickering aurora) and pulsating aurora is also quasi-periodic. Here we look at the response of a harmonic excitation-source that starts at time zero. $q(t)$ varies between q and zero.

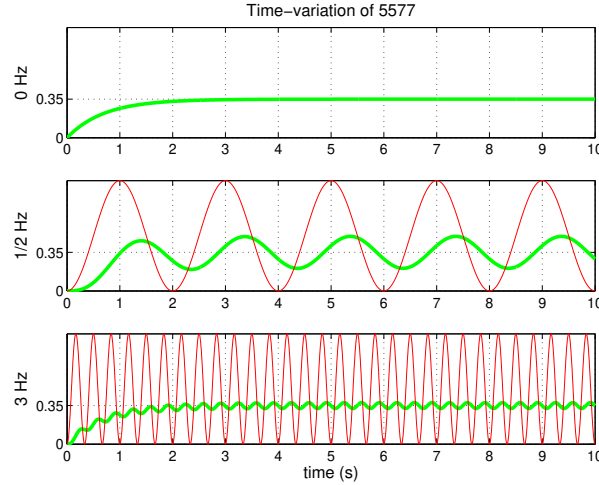
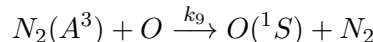


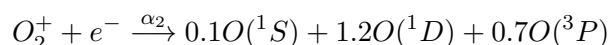
Figure 3.12: The time-variation of 5577 Å aurora produced by a excitation starting at time zero constant in time in the upper panel, harmonically modulated with 1/2 and X Hz in the middle and bottom panels.

When we integrate the $O(^1S)$ continuity-equation for onset of constant excitation we see the expected $1 - \exp(-t/0.7)$ growth characteristics, as show in the top panel, and for increasing frequency we see that the modulation amplitude decreases with increasing frequency - this can be understood simply by noting that when the 0.7 s life-time becomes long compared to the period-time of the excitation only a small fraction of the $O(^1S)$ excited during an excitation-peak have decayed before the next excitation peak starts.

General case with coupling to other sources So far simplified the $O(^1S)$ -equation to a single source. In reality we have additional sources of $O(^1S)$, energy-transfer from $N_2(A^3)$:



which is a dominant source in aurora, and dissociative recombination of O_2^+ :



meaning that approximately 10 per cent of the oxygen atoms resulting from dissociative recombination are excited in the $1S$ state.

$$\frac{\partial n^*(t)}{\partial t} = -\frac{n^*(t)}{\tau} + q(t)$$

Including these sources into the continuity equation for $O(^1S)$ we get

$$\frac{\partial n_{O1S}(t)}{\partial t} = -\frac{n_{O1S}(t)}{\tau_{O1S}} + q_{O1S}(t) + k_9 n_O n_{N2A}(t) + \alpha_2 n_e(t) n_{O_2^+}(t)$$

Therefore we now need to couple this equation with the continuity-equations for $N_2(A^3)$, O_2^+ and e^- :

$$\begin{aligned} \frac{\partial n_{N2A}(t)}{\partial t} &= -\frac{n_{N2A}(t)}{\tau_{N2A}} + q_{N2A}(t) \\ \frac{\partial n_{O_2^+}(t)}{\partial t} &= -\alpha_2 n_e(t) n_{O_2^+}(t) - k_{10} n_{N_2} n_{O_2^+}(t) - k_{12} n_{NO}(t) n_{O_2^+}(t) \\ &\quad + k_{11} n_{O_2} n_{N_2^+}(t) + k_{12} n_{O_2} n_{O^+} + q_{O_2^+}(t) \\ \frac{\partial n_{e^-}(t)}{\partial t} &= -\alpha_1 n_e(t) n_{NO^+}(t) - \alpha_2 n_e(t) n_{O_2^+}(t) - \alpha_3 n_e(t) n_{N_2^+}(t) \\ &\quad + q_{e^-}(t) \end{aligned}$$

The number-density of the major species, atomic oxygen, molecular oxygen and molecular nitrogen are not modified by ionization and the chemical reaction. The total ion-density is orders of magnitude smaller than the neutral densities so the minor variation does not change the speed of reactions.

If we look at the four coupled continuity equations above we see that with only the first two we have simple linear ODEs, however with the electron and molecular oxygen ion continuity equations we have two nonlinear ODEs that further couple to the rest of the ions (compare with programming-task #4), so the full ionospheric chemistry should be accounted for.

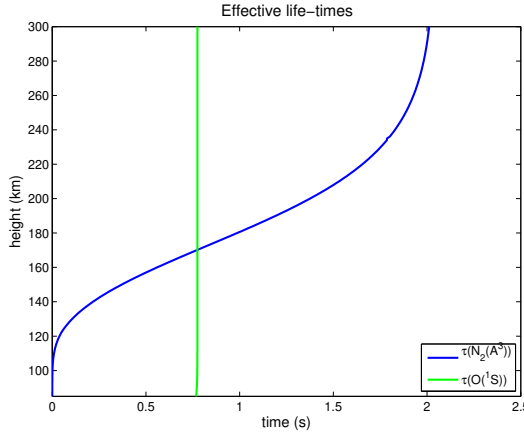


Figure 3.13: $O^+(2P)$ Altitude-variation of effective lifetimes of $O(1S)$ and $N_2(A^3)$

Looking at the altitude-variations of the effective lifetimes of $O(1S)$ and $N_2(A^3)$, shown in figure 3.13 we see that due to the short lifetime of $N_2(A^3)$ at altitudes below the 140 km, the time-variation of $N_2(A^3)$ and its contribution to $O(1S)$ would have a very small phase-shift relative to the direct electron-impact excitation.

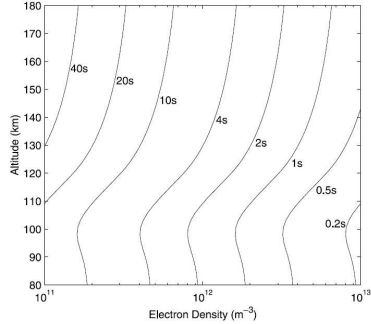


Figure 3.14: Isocontours of the ion recombination time, $\tau = 1/\alpha_{avg} n_e$ as function of plasma density and altitude, [from Semeter and Kamalabadi, 2005].

If we look at the electron-recombination-time, presented in figure 3.14, we see that for weaker aurora, when the electron-density does not exceed $5 \cdot 10^{11} / (\text{m}^3)$ the dissociative recombination is not a big source, it varies slowly compared to the O1S lifetime. However for more intensive aurora when the electron density grows higher in the E-region its variation becomes more rapid.

3.14 Molecular excitations

Since molecules has both electronic and vibrational energies the production of excited states are more complicated than for atomic states - primarily due to the fact that energy-levels for multiple electronic states with different vibrational excitation overlap, as shown in figure 3.15. To prepare for the calculation of the production of the different vibrational states of molecular nitrogen we will first analyse the simpler case of $O(1D)$.

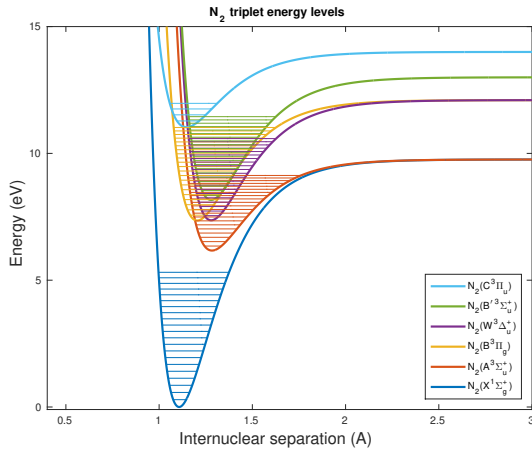


Figure 3.15: The energy-levels of the ground-state and the triplet-states of molecular nitrogen are plotted with the Morse-potential-curves illustrating how the vibrational states of the electronically excited states overlap.

Preparation for production of excited states of N_2 : $O(^1D)$ – again Before taking on the task of explaining the production of excited states of molecular nitrogen we take another look at the excitation of $O(^1D)$. Here we're going to look at the production of $O(^1D)$ by direct electron-impact excitation and by cascading from $O(^1S)$. $O(^1D)$ has multiple sources, for illustration of how to model many excited states that are coupled by cascading we look at only $O(^1D)$ and $O(^1S)$

$$\begin{aligned}\frac{\partial n_{O1D}(t)}{\partial t} &= -\frac{n_{O1D}(t)}{\tau_{O1D}} + q_{O1D}(t) + A_{5577}n_{O1S}(t) \\ \frac{\partial n_{O1S}(t)}{\partial t} &= -\frac{n_{O1S}(t)}{\tau_{O1S}} + q_{O1S}(t)\end{aligned}$$

The continuity equations for the two singlet-states we see that the $O(^1D)$ -continuity-equation depends on the $O(^1S)$ equation. Therefore they should be solved together. This system of coupled ODEs can be rewritten in matrix form to

$$\frac{\partial}{\partial t} \begin{bmatrix} n_{O1D}(t) \\ n_{O1S}(t) \end{bmatrix} = \begin{bmatrix} -1/\tau_{O1D} & A_{5577} \\ 0 & -1/\tau_{O1S} \end{bmatrix} \begin{bmatrix} n_{O1D}(t) \\ n_{O1S}(t) \end{bmatrix} + \begin{bmatrix} q_{O1D}(t) \\ q_{O1S}(t) \end{bmatrix}$$

For steady-state conditions this leads to a solution for the excited densities by multiplying the excitation-rates with the inverse of the matrix with the inverse of the effective life-times along the diagonal (remember that $1/\tau$ simplifies to the sum of the Einstein coefficients in the low-collision-case) and the negative of the cascading-contributions in the correct position.

For steady-state conditions we see that the number-density of $O(^1D)$ and $O(^1S)$ are obtained by multiplying the array of productions with the inverse of the matrix in the equation above:

$$\begin{bmatrix} n_{O1D}(t) \\ n_{O1S}(t) \end{bmatrix} = \begin{bmatrix} 1/\tau_{O1D} & -A_{5577} \\ 0 & 1/\tau_{O1S} \end{bmatrix}^{-1} \begin{bmatrix} q_{O1D}(t) \\ q_{O1S}(t) \end{bmatrix}$$

This is the simplest case of the solution of coupled continuity-equations for multiple excited states where there are cascading from states with higher energy to lower.

Molecular excitations: N₂-triplet system

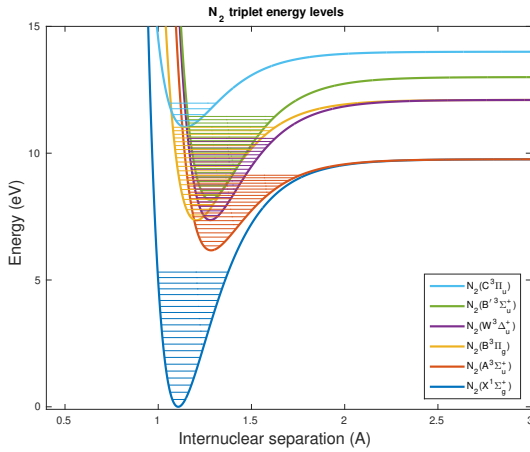


Figure 3.16: The energy-levels of the ground-state and the triplet-states of molecular nitrogen are plotted with the Morse-potential-curves illustrating how the vibrational states of the electronically excited states overlap.

If we look at the triplet-states of molecular nitrogen ($A^3\Sigma_u^+$, $B^3\Pi_g$, $W^3\Delta_u^+$, $B'^3\Sigma_u^+$ and $C^3\Pi_u$) we see that there are a number of overlapping vibrational levels. Here transitions can go from each electronic-vibrational level to all lower levels, which would be a large number of transitions between the different states. However, the selection-rule for allowed transitions (electric dipole transition) are that it has to be a transition between from an odd (u for umgerade) to an even (g for gerade) state or the other way around (see: Laporte rule). For the N_2 triplet states this means that there will only be transitions from the u-states $A^3\Sigma_u^+$, $W^3\Delta_u^+$, $B'^3\Sigma_u^+$ and $C^3\Pi_u$) to the $B^3\Pi_g$ state and from the $B^3\Pi_g$ -state to the others. The energy-levels of the $A^3\Sigma_u^+$, $B^3\Pi_g$, $W^3\Delta_u^+$, $B'^3\Sigma_u^+$ states are jumbled and there will be transitions between the different electronic states, effectively there will be cascading from all energy-levels in ($A^3\Sigma_u^+$, $W^3\Delta_u^+$, $B'^3\Sigma_u^+$ and $C^3\Pi_u$) to a vibrational level of $B^3\Pi_g$ if it is at a lower energy-level, and from each vibrational level of $B^3\Pi_g$ there will be cascading down to each vibrational level of ($A^3\Sigma_u^+$, $B^3\Pi_g$, $W^3\Delta_u^+$, $B'^3\Sigma_u^+$ and $C^3\Pi_u$ at lower energy-levels.

Populating the N₂-triplet states

Molecular excitations: Band-systems II Taking into account all the allowed transitions between the different vibrational levels of the major triplet-states the

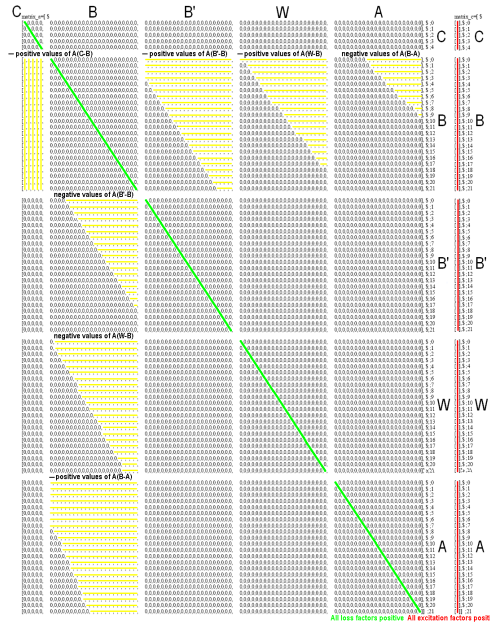


Figure 3.17: Schematic structure of the transition-matrix \mathbf{M} and the excitation-vector $\mathbf{q}_{N_2(3)}$, from [Jokiah, 2009].

coupled continuity-equations becomes a similar system of equations as for the coupled continuity-equations for $O(^1D)$ and $O(^1S)$, except that here there are a larger number of coupled equations:

$$\frac{\partial \mathbf{n}_{N_2(3)}}{\partial t} = -\mathbf{M} \cdot \mathbf{n}_{N_2(3)} + \mathbf{q}_{N_2(3)}$$

where $\mathbf{n}_{N_2(3)}$ and $\mathbf{q}_{N_2(3)}$ are column-vectors with the local number-density and excitation of all the vibrational states of the five triplet-states of molecular nitrogen, and \mathbf{M} is the transition-matrix. Since all transitions except the lowest vibrational levels of the A^3 -state have large Einstein coefficients (short life-times) we treat this equation with a steady-state assumption. This gives us the densities:

$$\mathbf{n}_{N_2(3)} = \mathbf{M}^{-1} \cdot \mathbf{q}_{N_2(3)}$$

The \mathbf{M} and \mathbf{M}^{-1} matrices

Here we note that the diagonal elements of the transfer matrix is negative (corresponding to losses) while the off-diagonal elements are positive (corresponding to sources)

Here we see that all components of the inverse are positive, which makes sense since the contributions to every vibrational state of all triplet-states from excitation of any vibrational level of any triplet-state are either positive or zero.

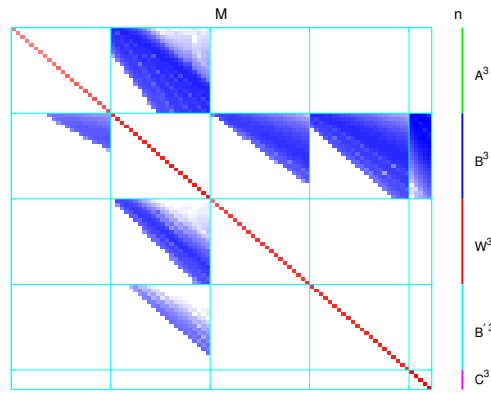


Figure 3.18: Structure of the transition-matrix \mathbf{M} and the excitation-vector $\mathbf{q}_{N_2(3)}$

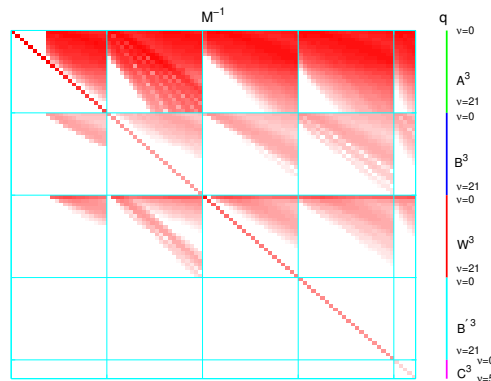


Figure 3.19: Structure of \mathbf{M}^{-1} i.e. the inverse of the transition-matrix and the excitation-vector $\mathbf{q}_{N_2(3)}$

Population of vibrational levels

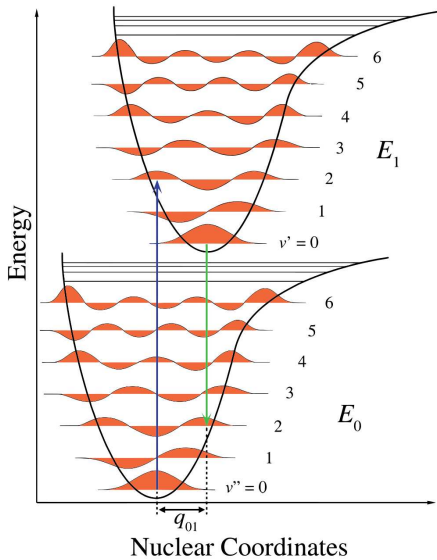


Figure 3.20: Illustration for the Frank-Condon principle with the vibrational wave-functions for Morse-potentials of two electronically excited states.

The population of the vibrational levels of an electronically excited state can be calculated using the Franck-Condon principle. It is based on the observation that the time of the electronic transition from the electronic ground-state to the electronically excited state is very short compared to the time-scale of the vibrational oscillations of the nuclei, or in simpler terms when a nitrogen molecule goes from the ground-state to an excited state the separation between the nuclei does not change. Since the ground-state and the excited state might have different equilibrium distance, and different Morse-potentials. The population between the different vibrational levels are then proportional to

$$p(\nu) \propto \int \psi'^*\psi_0 dV$$

where $\psi'^*\nu$ is the complex conjugate of the ν -th vibrational wave-function of the excited state and ψ_0 is the 0-th level vibrational wave-function of the ground-state molecule.

In a simplified picture we can take the amplitudes of the vibrational wave-functions of the excited state at the equilibrium separation of the ground-state (that's the separation of the atoms in the excited molecules will have just after the excitation) and partition the molecules between the states according to those.

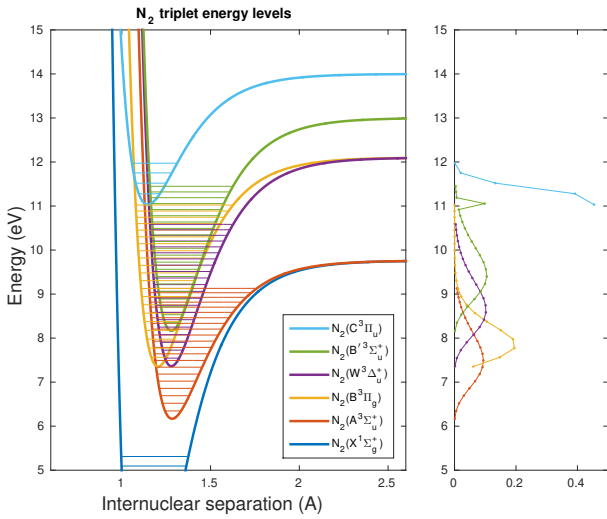


Figure 3.21: Triplet-states of molecular nitrogen in the left panel with the corresponding Frank-Condon-factors in the right panel.

Partition of Vibrational States

The partition between the vibrational states of the N₂-triplet-states have been calculated [Gilmore *et al.*, 1992] and are presented beside the energy-level diagram. For the A^3 state the most probable vibrational states are the 7th and 8th, the most probable states for B^3 are the 2nd and 3rd, for the W^3 -state the vibrational distribution peaks at the 7th level, for the B'^3 state peaks at the 7th too, but has a peculiar peak at the 18th vibrational level, while the C^3 state is mainly populated at the 0th and 1st vibrational level.

3.15 Time-of-flight effects

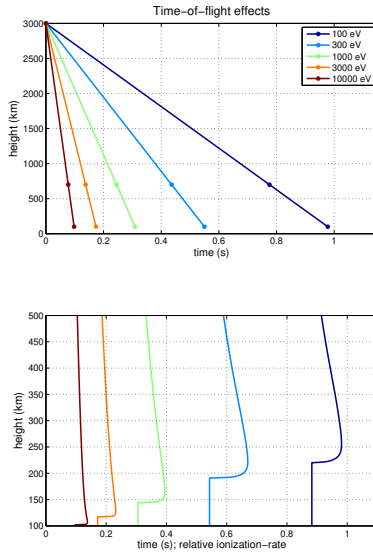


Figure 3.22: 10

For time-variations on scales shorter than 0.3-0.5 s the steady-state assumption for electron-transport starts to be problematic. That is, after an onset of electron-precipitation at some source-altitude above the top of the ionosphere there will be a spread of arrival-times for electrons with different energies, due to the corresponding difference in velocity and time-of-travel, and electrons with the same energy but different initial pitch-angle, due to different length-of-trajectory.

In addition to the energy-time-dispersion secondary electrons at lower altitudes will lose their energy faster, since the larger neutral density leads to shorter time between inelastic collisions at lower altitudes, above 200 km the energy-degradation-time becomes longer.

3.16 Effects on prompt emissions

The altitude and time-variations of prompt emissions will start to display similar variation as the forbidden transitions (for example the 7320-7330 and 6300 Å emission discussed earlier), but on shorter time-scales. This is not due to the life-time, but due to the time-variations of the electron-fluxes.

Cross-sections and fluxes

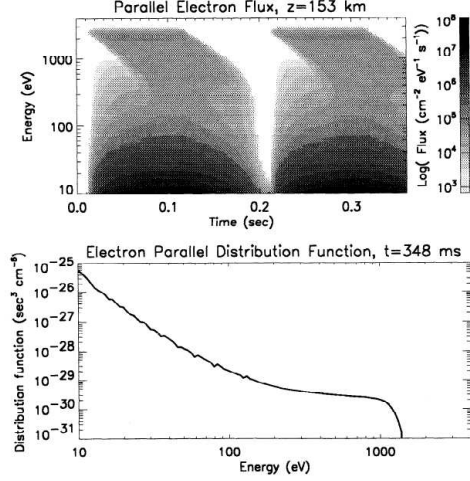


Figure 3.23: The top panel shows the time-energy variation of electron-energy-flux at 153 km of altitude where the time-dispersion of the primary electrons with energies above a few 100 eV is clearly visible as is the effect of the time-varying production and energy degradation of the secondary electrons at energies below 100 eV. 11

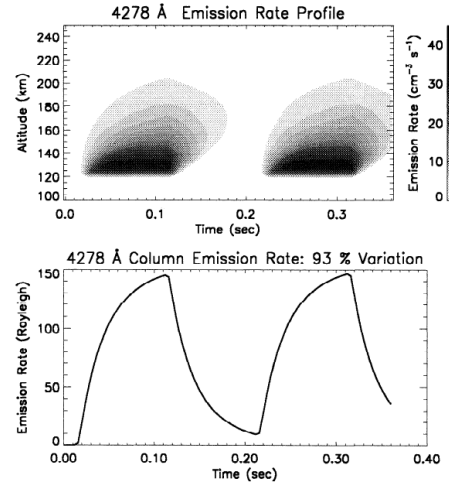


Figure 3.24: The top panel shows the altitude-time-variation of volume-emission-rate at 4278 Å from molecular nitrogen ions calculated with the first time-dependent electron transport code by Peticolas and Lummerzheim [2000]. The bottom panel displays the corresponding column emission-rates. 12

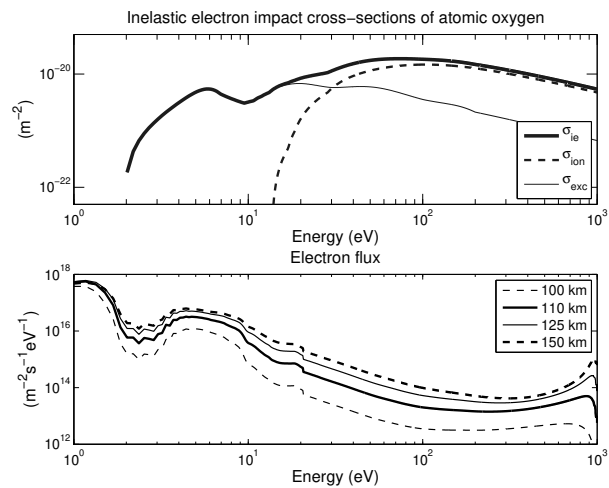


Figure 3.25: In the top panel the total elastic, ionizing and other inelastic electron impact collision cross-sections are plotted as functions of energy. This illustrates that at energies above approximately 100 eV the ionization-cross-sections are roughly 50 times larger than all the other inelastic cross-sections combined.

Chapter 4

Precipitation-processes

M-I Coupling Processes There are three main types of auroral precipitation (very coarsely grouped). They differ in the processes that cause the precipitation from the magnetosphere into the ionosphere and also due to their different spatial and temporal dynamics in the spatial and temporal variation of the auroral emissions that are generated. The three groups are pitch-angle scattering, quasistatic acceleration and alfvénic acceleration. These three groups of precipitation lead to “diffuse aurora”, “stable auroral arcs” and “dynamic aurora”, respectively.

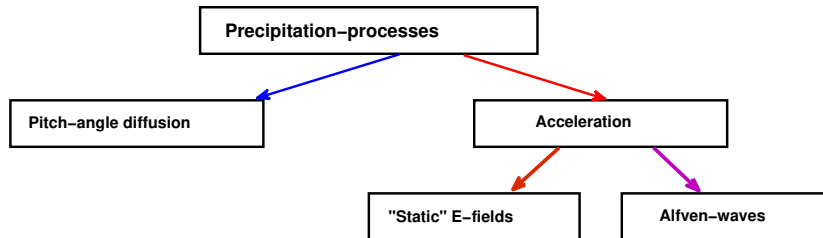


Figure 4.1: Grouping of precipitation processes.

4.1 Diffuse Aurora

The diffuse aurora is typically a less bright aurora with larger extent. It is an often occurring faint glow that covers the entire auroral oval, it typically extends equatorward of discrete

auroral structures as seen in figure 4.2. Due to the large area covered with diffuse aurora the total energy-flux in the diffuse aurora is larger than the energy-flux in the discrete aurora. Despite its name there are often regions of diffuse aurora with small-scale structures, one example shown in figure 4.3, the smallest structures are found in the diffuse aurora (Ref to Partamies) – the label is a miss-nomer in describing the structures of the aurora.

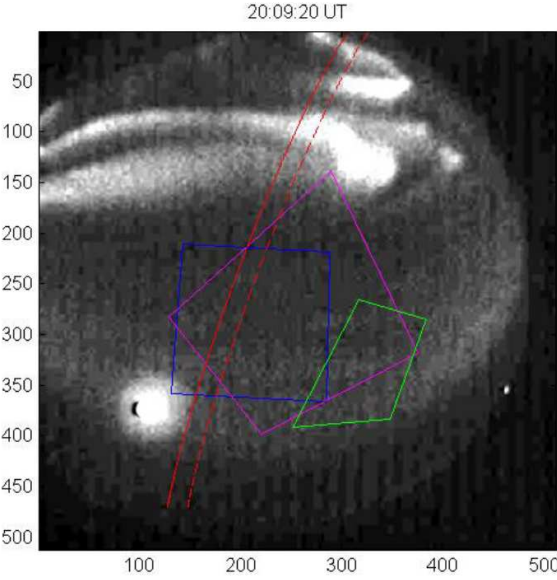


Figure 4.2: Diffuse aurora captured with the all-sky camera in Kiruna 19970216 with the fields-of-view of the ALIS cameras in Kiruna (b), Nikkaluokta (v) and Merasjärvi (g) overlaid together with the FAST satellite ionospheric footpoint trajectory, from Sergienko *et al.* [2008].

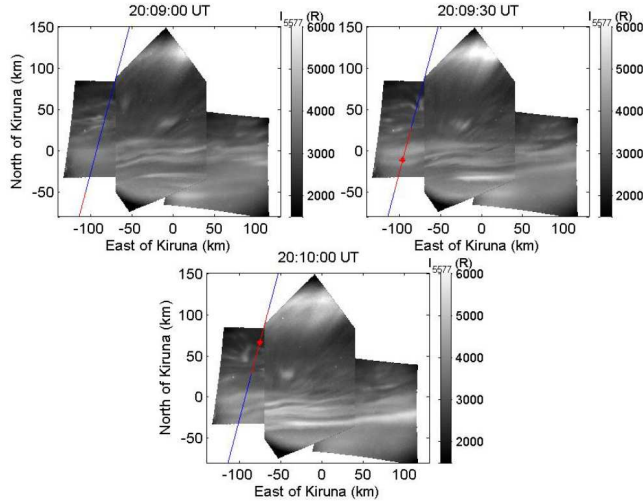


Figure 4.3: ALIS images of diffuse aurora with small-scale structures projected to 100 km of height with the FAST footpoints overlayed, from Sergienko *et al.* [2008].

However, the mechanism causing the precipitation is consistent across the different scale-sizes and separate from the other groups. The precipitation is caused by pitch-angle scattering of trapped high-energy electrons, without significant field-aligned acceleration, as shown in the simultaneously observed electron energy-spectrum

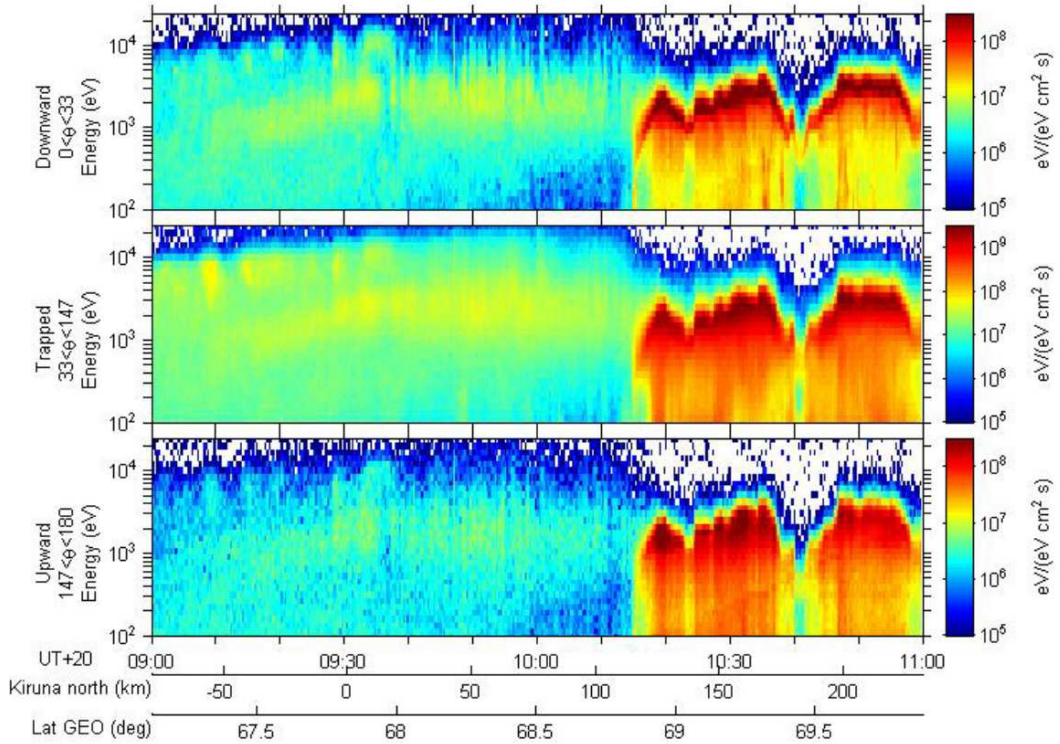


Figure 4.4: FAST electron spectrograms from 19970216 showing the small-scale structuring of the diffuse precipitation most pronounced south of 68° . Notice the difference both in low-energy fluxes and width of the high-energy component compared to the accelerated “inverted-V” precipitation north of 68.8° , from Sergienko *et al.* [2008].

shown in figure 4.4). The electrons causing the diffuse aurora is in general well described by a Maxwellian energy-spectrum, as shown in figure 4.5.

The pitch-angle scattering of trapped electrons into the loss-cones are thought to be caused by whistle-waves and ion-cyclotron-waves. At times there can be a quasi-periodic variation of the diffuse precipitation leading to “pulsating aurora”, with typical period-times of between 3 and some 10s of seconds. The intensity-variation of the pulsations often have a close to on-off characteristics.

4.1.1 Black Aurora

In addition to the small-scale bright structures and the pulsations there are also regions with reduced luminosity. These darker regions comes in patch-like structures, roughly east-west aligned “arcs”, as shown in figure 4.6 and even rings. This type of aurora have been named “black aurora”, and are caused by reduce pitch-angle scattering of high-energy electrons as shown in figure 4.7.

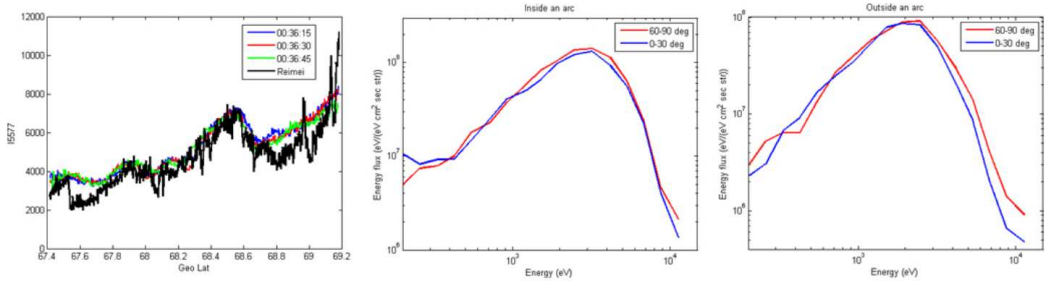


Figure 4.5: Diffuse auroral brightness and electron spectrograms, note how Maxwellian the electron spectra in the middle and right panels are, from [Axelsson et al. 20XX](#).

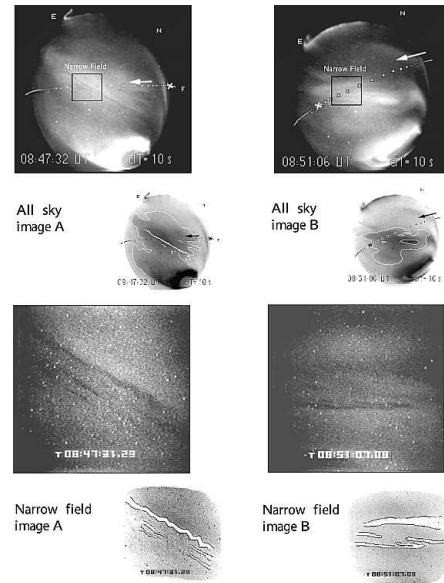


Figure 4.6: All-sky and medium field-of-view imaging of diffuse aurora with narrow regions of slightly reduced luminosity - traditionally named “black aurora”, from [Peticolas et al. \[2002\]](#).

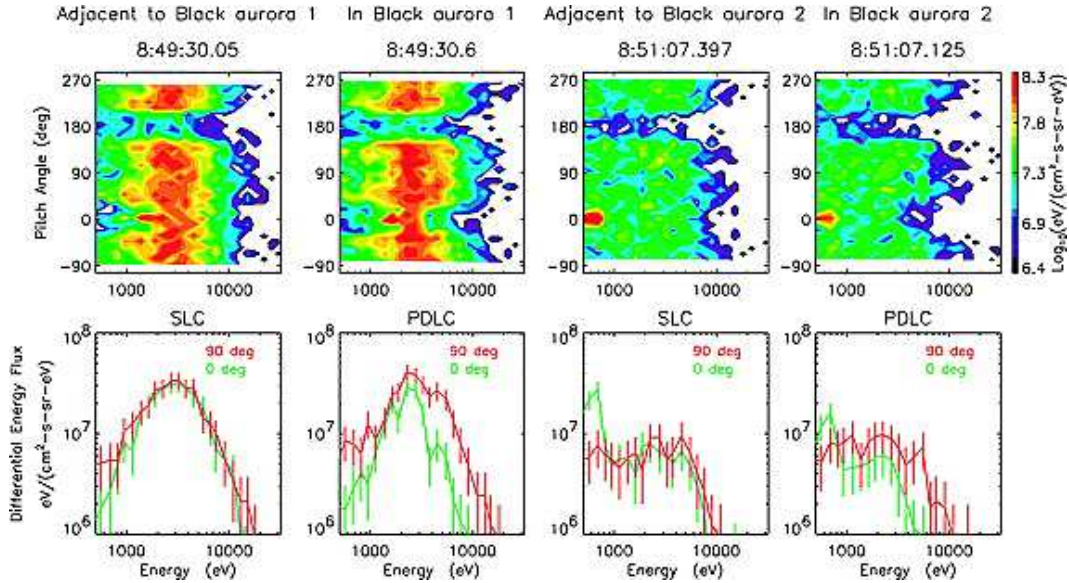


Figure 4.7: Pitch-angle–energy spectrogram of electrons above black aurora where the reduced fluxes in the loss-cone around 180° can be seen in the four top panels. The difference in the downward fluxes around 0° are noticeable at energies above some 2 keV for the 8:49:30 case. Note how similar the electron fluxes are in the trapped populations next to an inside the black aurora and in the trapped and precipitating populations in the black aurora. This rules out retarding electrical fields as a cause of “black aurora” - since that would lead to an identical energy-loss of all electrons at all energies and pitch-angles. From Peticolas *et al.* [2002].

4.2 Quasistatic Acceleration

Above stable auroral arcs regions of upward directed electrical fields are found. These electrical potential-structures accelerates all electrons from the magnetospheric (high-altitude) side with an energy corresponding to the potential-difference, as shown in the top-panel of figure 4.9. These high-energy-fluxes often appear as “inverted-V” in electron-energy-flux plots which gave this type of precipitation its label. In addition to the narrow-energy, often labeled “mono-energetic”, high-energy flux there is a low-energy-tail which has its origin from secondary electrons that has escaped the ionosphere and has been reflected/mirrored back down when encountering the electrical potential-structure.

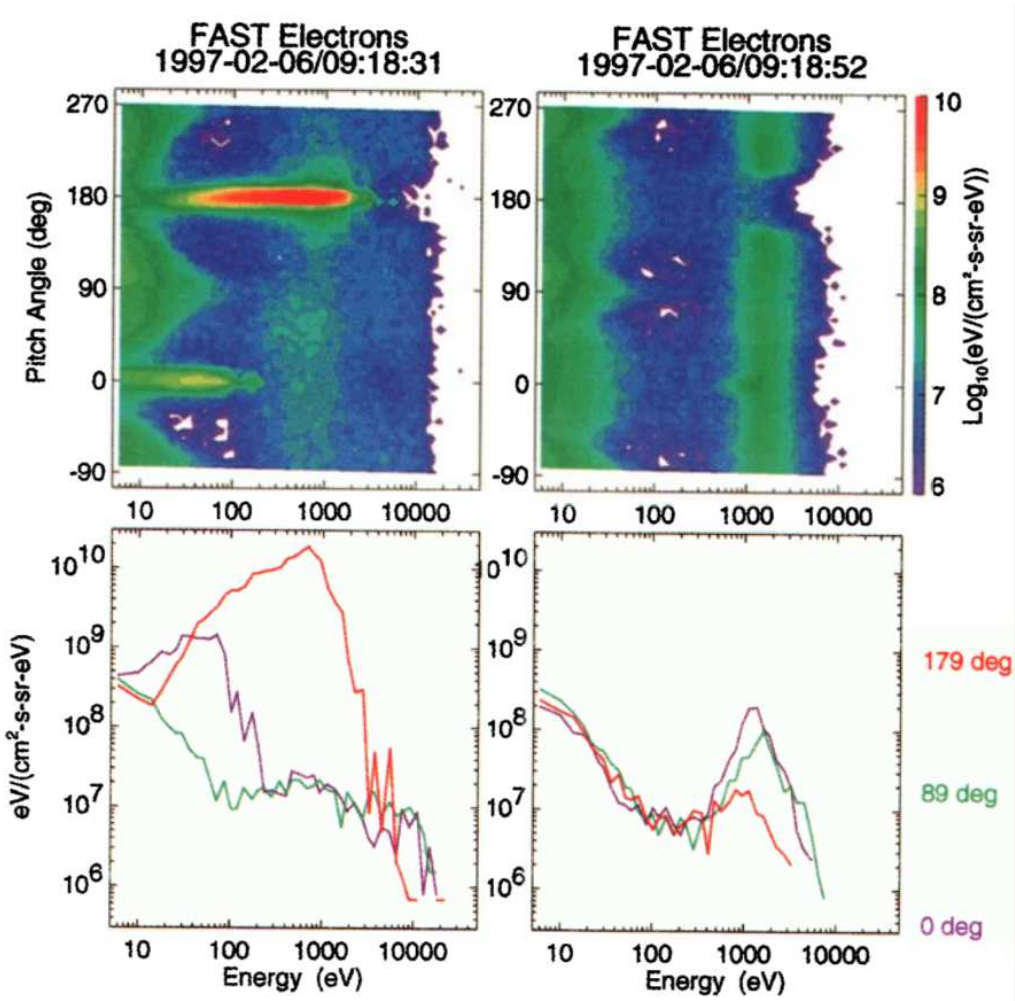


Figure 4.8: FAST observations of pitch-angle-resolved electron-energy-fluxes in the downward current region in the left panels and in the upward current region in the right panels. In the downward current region a narrow beam of electrons can be seen at energies up to approximately 1 keV, while in the upward current region there is a 1-2 keV “monoenergetic” population that covers all pitch-angles except in the narrow loss-cone around 180°. In addition there is a nearly isotropic flux of low-energy electrons with energies below 100 eV. From *McFadden et al.* [1999].

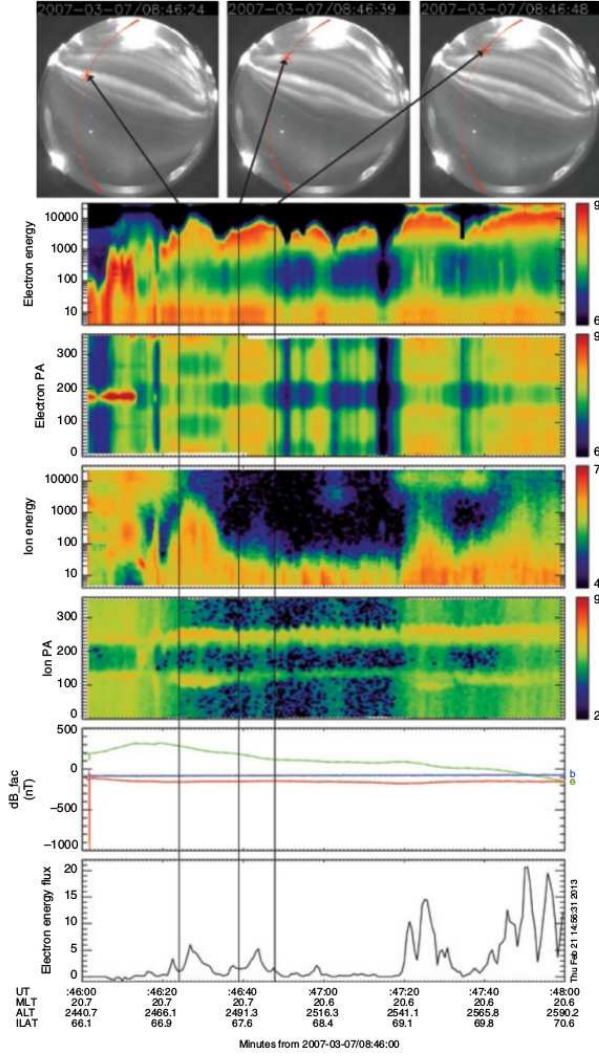


Figure 4.9: An example of inverted-V-precipitation above stable auroral arcs. In the top three panels all-sky images of a multi-arc system is displayed with the footpoints of the FAST satellite overlayed in red. The times corresponding to the arc-passings are marked in the electron-energy spectrogram (second row), the electron pitch-angle spectrogram (third row) and the ion energy and pitch-angle spectrograms (in the fourth and fifth row), and the magnetic field and electron energy variation in the two last panels. **Colpitts, fig 1.3 Chapter 1, Auroral dynamics and space weather ed: Zhang and Paxton**

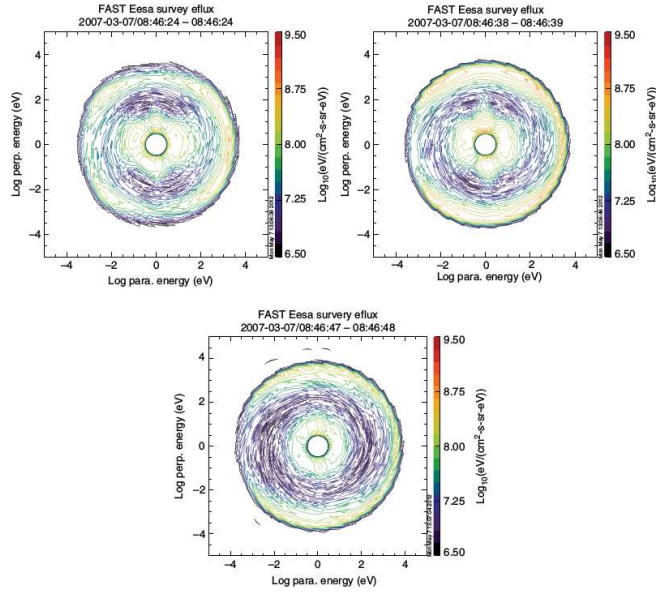


Figure 4.10: Three examples of the characteristic Horse-shoe distributed electrons that arise from an electrostatic acceleration followed by the pitch-angle widening due to the conservation of both the total energy and magnetic moment of electrons as they precipitate down into stronger magnetic fields. From Colpitts *et al.* [2013].

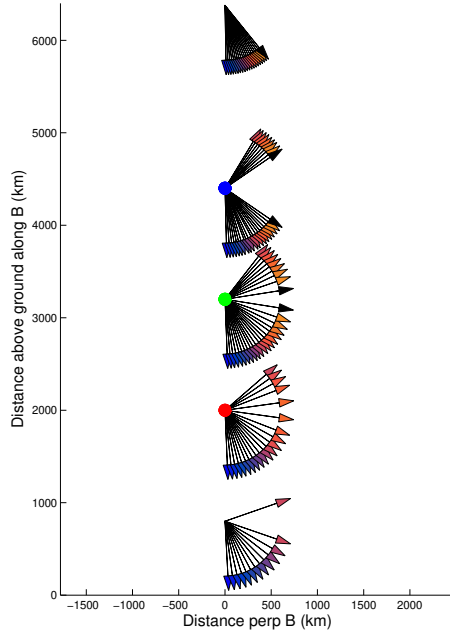


Figure 4.11: Cartoon illustrating the pitch-angle widening effect of the magnetic mirror-force

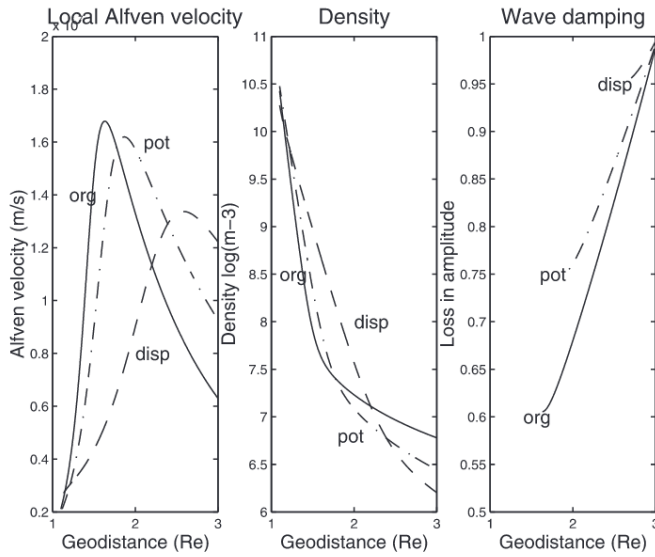


Figure 4.12: The left panel show the altitude-variation the Alfven-wave for three plasma-density-profiles. The altitude of peak v_A varies by more than $1 R_e$ depending on the plasma-density-profile, shown in the midle panel. The different altitude-variations has a consequence on the damping of the waves, as shown in the right panel. From *Andersson et al.* [2002].

4.3 Alfvénic acceleration

Another process that can cause precipitation is the interaction between Alfvén waves and electrons in the magnetosphere. In the magnetosphere where the magnetic field both curves and changes in strength and the plasma-density varies along the magnetic field-lines the Alfvén velocity, v_A , varies with height. This gives the waves an electric-field-component along the field-line.

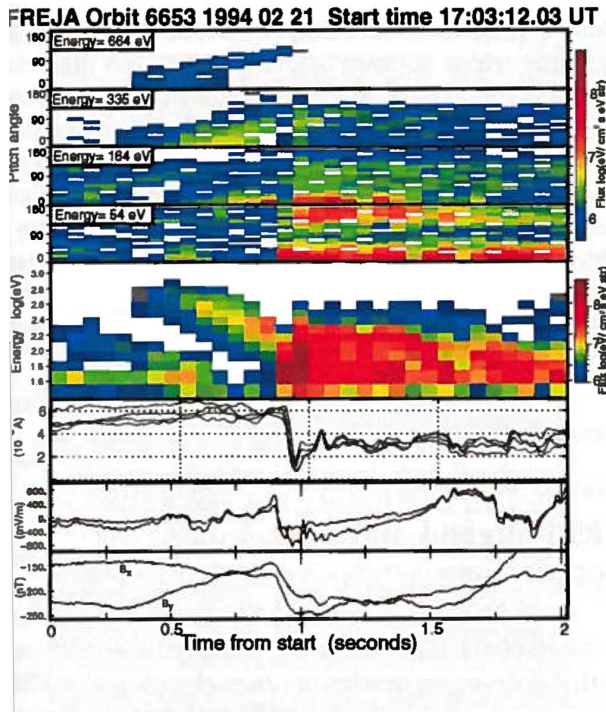


Figure 4.13: Alfvén-wave accelerated electron-spectra

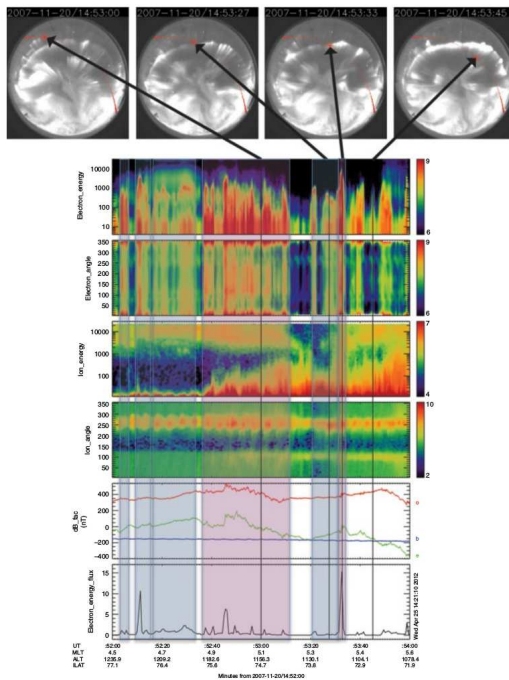


Figure 4.14: Examples of Alfvénic precipitation, Colpitts *et al.* [2013]

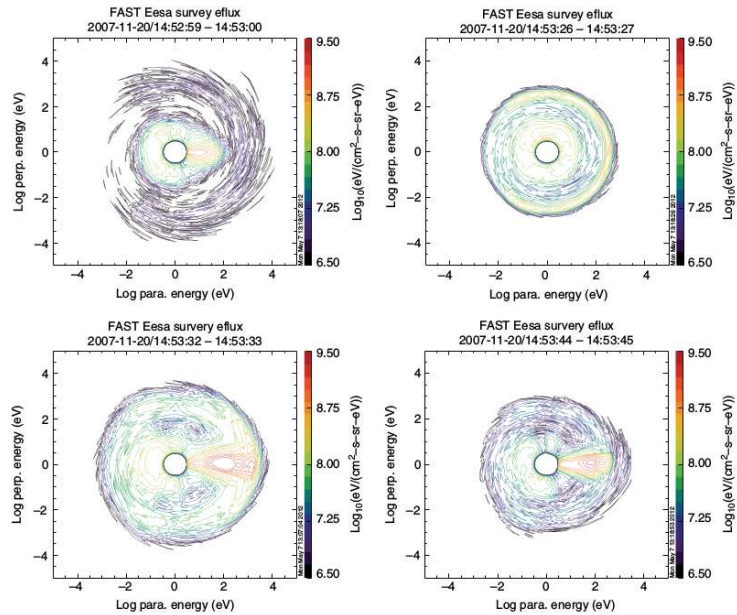


Figure 4.15: Pitch-angle resolved electron-energy-fluxes with wide energy-distributed field-aligned beams in panels 1, 3 and 4 to be contrasted to the mono-energetic horse-shoe distributed energy-flux in panel 2. From Colpitts *et al.* [2013].

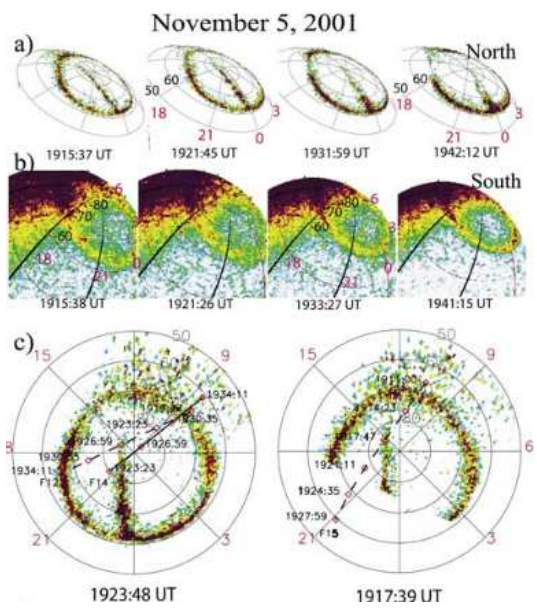


Figure 4.16: Simultaneous observations of polar-cap arcs from the northern and southern auroral ovals. From Østgaard *et al.* [2003].

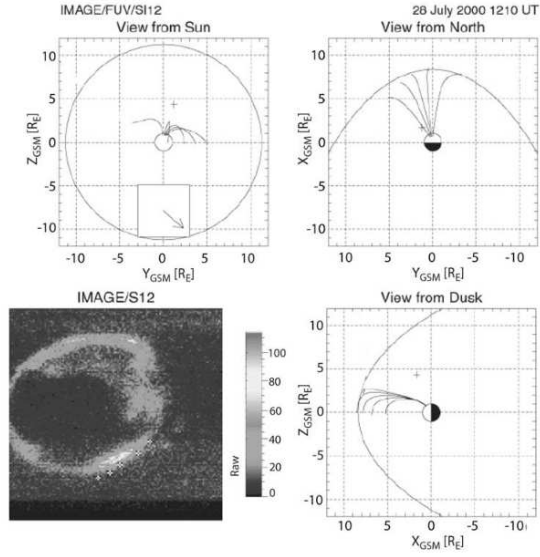


Figure 4.17: Cusp aurora and the corresponding magnetic-field-line tracings to the day-side magnetopause for the IMF B_z negative case. From *Fuselier et al.* [2002].

4.4 Other Auroras

Cusp Aurora

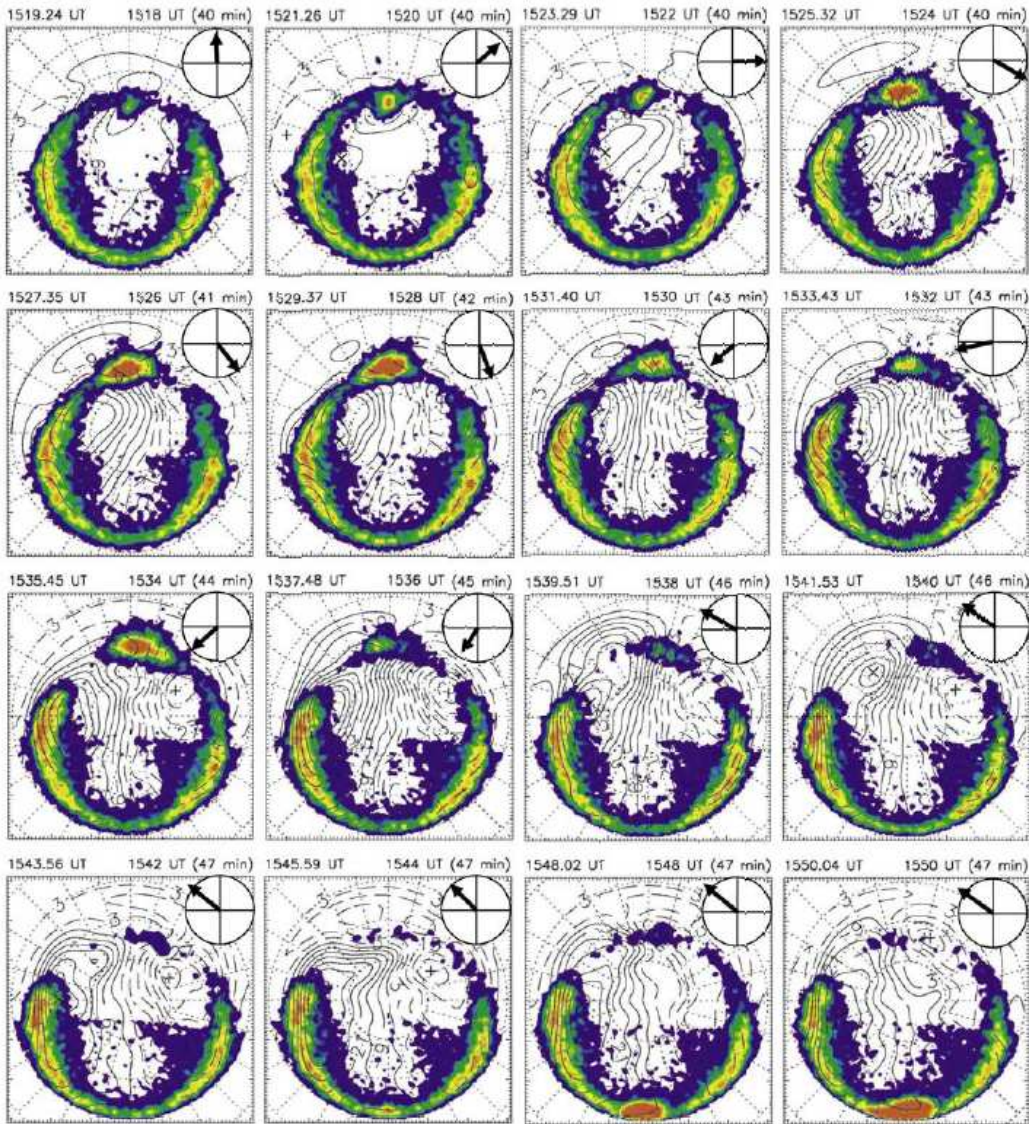


Figure 4.18: The interplanetary magnetic-field impact on the location and intensity of cusp proton aurora. From *Lockwood et al. [2003]*.

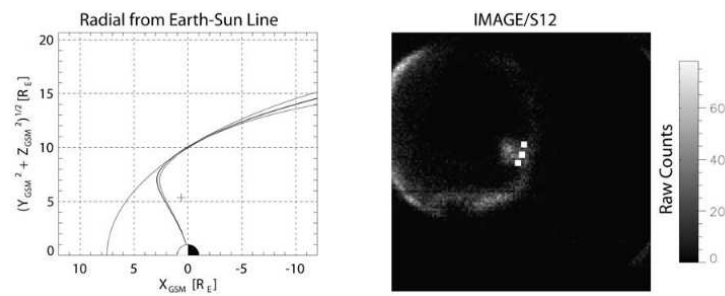


Figure 4.19: Cusp aurora and the corresponding magnetic-field-line tracings to the day-side magnetopause for the IMF B_z positive case. From Frey [2007].

Bibliography

- Andersson, L., N. Ivchenko, J. Clemons, A. A. Namgaladze, B. Gustavsson, J.-E. Wahlgren, L. Eliasson, and R. Y. Yurik, Electron signatures and Alfvén waves, *J. Geophys. Res.*, **107**, 15–1, 2002.
- Colpitts, C. A., S. Hakimi, C. A. Cattell, J. Dombeck, and M. Maas, Simultaneous ground and satellite observations of discrete auroral arcs, substorm aurora, and alfve'nic aurora with fast and themis gbo, *J. Geophys. Res. Space Physics*, **118**, 6998–7010, 2013.
- Frey, H. U., Localized aurora beyond the auroral oval, *Rev. Geophys.*, **45**, RG1003, 2007.
- Fuselier, S. A., H. U. Frey, K. J. Trattner, S. B. Mende, and J. L. Burch, Cusp aurora dependence on interplanetary magnetic field b_z , *J. Geophys. Res.*, **107**, 1111, 2002.
- Gilmore, F. R., R. R. Laher, and P. J. Espy, Franck-Condon factors, r-Centroids, electronic transition moments, and Einstein coefficients for many nitrogen and oxygen band systems, *J. Phys. Chem. Ref. Data*, **21**, 1005–1107, 1992.
- Gronoff, G., C. Simon Wedlund, C. J. Mertens, and R. J. Lillis, Computing uncertainties in ionosphere-airglow models: I. electron flux and species production uncertainties for mars, *J. Geophys. Res.*, **117**, A04,306, 2012.
- Gustavsson, B., Three Dimensional Imaging of Aurora and Airglow, Ph.D. thesis, Swedish Institute of Space Physics, Kiruna, Sweden, 2000, (IRF Sc.i Report 267), ISBN: 91-7191-878-7.
- Hecht, J. H., A. B. Christensen, D. J. Strickland, and R. R. Meier, Deducing composition and incident electron spectra from ground-based auroral optical measurements: Variation in oxygen density, *J. Geophys. Res.*, **94**, 13,553–13,563, 1989.
- Itikawa, Y., and A. Ichimura, Cross sections for collisions of electrons and photons with atomic oxygen, *J. Phys. Chem. Ref. Data*, **19**, 637–651, 1990.
- Itikawa, Y., M. Hayashi, A. Ichimura, K. Onda, K. Sakimoto, K. Takayanagi, M. Nakamura, H. Nishimura, and T. Takayanagi, Cross sections for collisions

of electrons and photons with nitrogen molecules, *J. Phys. Chem. Ref. Data*, *15*, 985–1010, 1986.

Itikawa, Y., A. Ichimura, K. Onda, K. Sakimoto, K. Takayanagi, Y. Hatano, M. Hayashi, H. Nishimura, and S. Tsurubuchi, Cross Sections for Collisions of Electrons and Photons with Oxygen Molecules, *Journal of Physical and Chemical Reference Data*, *18*, 23–42, 1989.

Jokiah, O.-P., Spectral modelling of molecular nitrogen in aurora, Ph.D. thesis, University of Southampton, 2009.

Lockwood, M., B. S. Lanchester, H. U. Frey, K. Throp, S. K. Morley, S. E. Milan, and M. Lester, Imf control of cusp proton emission intensity and dayside convection: Implications for component and anti-parallel reconnection, *Ann. Geophys.*, *21*, 955–982, 2003.

McFadden, J. P., C. W. Carlson, and R. E. Ergun, Microstructure of the auroral acceleration region as observed by fast, *J. Geophys. Res.*, *104*, 14,453–14,480, 1999.

Meier, R. R., D. J. Strickland, J. H. Hecht, and A. B. Christensen, Deducing composition and incident electron spectra from ground-based auroral optical measurements: A study of auroral red line processes, *J. Geophys. Res.*, *94*, 13,541–13,552, 1989.

Opal, C., E. Beaty, and W. Peterson, Tables of secondary-electron-production cross sections, *Atomic Data and Nuclear Data Tables*, *4*, 209–253, 1972.

Østgaard, N., S. B. Mende, H. U. Frey, L. A. Frank, and J. B. Sigwarth, Observations of non-conjugate theta aurora, *Geophys. Res. Lett.*, *30*, 2125, 2003.

Otsuka, Y., K. Shiokawa, T. Ogawa, and P. Wilkinson, Geomagnetic conjugate observations of equatorial airglow depletions, *Geophysical Research Letters*, *29*, 43–1, 2002.

Peticolas, L., and D. Lummerzheim, Time-dependent transport of field-aligned bursts of electrons in flickering aurora, *J. Geophys. Res.*, *105*, 12,895–12,906, 2000.

Peticolas, L. M., T. J. Hallinan, H. C. Stenbaek-Nielsen, J. W. Bonnell, and C. W. Carlson, A study of black aurora from aircraft-based optical observations and plasma measurements on fast, *J. Geophys. Res.*, *107*, 2002.

Rees, M. H., *Physics and chemistry of the upper atmosphere*, Cambridge and New York, Cambridge University Press, 297 p., 1989.

Rees, M. H., and D. Luckey, Auroral electron energy derived from ratio of spectroscopic emissions 1. model computations, *J. Geophys. Res.*, *79*, 5181–5186, 1974.

- Rees, M. H., and D. Lummerzheim, Characteristics of auroral electron precipitation derived from optical spectroscopy, *J. Geophys. Res.*, *94*, 6799–6815, 1989.
- Sakanoi, K., and K. Fukunishi, Temporal and spatial structures of flickering aurora derived from high-speed imaging photometer observations at Syowa Station in the Antarctic, *J. Geophys. Res.*, *109*, 2004.
- Semeter, J., Ground based tomography of atmospheric optical emissions, Ph.D. thesis, Boston University, Boston, MA, 1997.
- Semeter, J., and F. Kamalabadi, Determination of primary electron spectra from incoherent scatter radar measurements of the auroral E region, *Radio Sci.*, *40*, 2005.
- Sergienko, T., I. Sandahl, B. Gustavsson, L. Andersson, U. Brändström, and Å. Steen, A study of fine structure of diffuse aurora with ALIS-FAST measurements, *Annales Geophysicae*, *26*, 3185–3195, 2008.
- Solomon, S. C., P. B. Hays, and V. J. Abreu, The auroral 6300 Å emission: Observation and modelling, *J. Geophys. Res.*, *93*, 9867–9882, 1988.
- Strickland, D. J., R. R. Meier, J. H. Hecht, and A. B. Christensen, Deducing composition and incident electron spectra from ground-based auroral optical measurements: theory and model results, *J. Geophys. Res.*, *94*, 13,527–13,539, 1989.
- Tuttle, S., B. Gustavsson, and B. Lanchester, Temporal and spatial evolution of auroral electron energy spectra in a region surrounding the magnetic zenith, *Journal of Geophysical Research: Space Physics*, *119*, 2318–2327, 2014.
- Whiter, D. K., B. S. Lanchester, B. Gustavsson, N. Ivchenko, and H. Dahlgren, Using multispectral optical observations to identify the acceleration mechanism responsible for flickering aurora, *J. Geophys. Res.*, *115*, 2010.

Index

- aiglow, 11
- aurora, 11
- cascading, 33
- collision cross-section, ionization, 25
- collision cross-section, ellastic, 25
- collision cross-section, inellastic, 25
- dissociation-energy, 17
- Einstein coefficient, 14
- electron impact excitation, 23
- Electron transport, 24
- equilibrium separation, 17
- excitation rate, 23
- excitation threshold, 23
- excitation-cross-section, 23
- molecular rotation, 18
- molecular vibration, 17
- Monte Carlo modeling, 24
- Morse-potential, 17
- multi-stream electron-transport, 34
- N2 first negative band, 19
- N2 first positive band, 19
- N2 Meinel band, 19
- N2 second positive band, 19
- O(1D), 14
- O(1S), 14
- P-branch, 19
- phase-function, 25
- pitch-angle-cosine, 28
- selection rules, 14, 19
- transition-probabilities, 14
- two-stream equation, 33
- vibrational levels, 17